

Water Resources Research

RESEARCH ARTICLE

10.1029/2020WR028734

Key Points:

- We developed a numerical solver to model multiphase flow through and around deformable porous media
- The model replicates the Volume-of-Fluid approach and multiphase Biot Theory with a single equation
- This open-source model can simulate complex phenomena including fracturing in ductile porous media

Supporting Information:

- Supporting Information S1

Correspondence to:

F. J. Carrillo,
franjcf@princeton.edu

Citation:

Carrillo, F. J., & Bourg, I. C. (2021). Modeling multiphase flow within and around deformable porous materials: A Darcy-Brinkman-Biot approach. *Water Resources Research*, 57, e2020WR028734. <https://doi.org/10.1029/2020WR028734>

Received 8 SEP 2020

Accepted 18 DEC 2020

Modeling Multiphase Flow Within and Around Deformable Porous Materials: A Darcy-Brinkman-Biot Approach

Francisco J. Carrillo¹  and Ian C. Bourg^{2,3}

¹Department of Chemical and Biological Engineering, Princeton University, Princeton, NJ, USA, ²Department of Civil and Environmental Engineering, Princeton University, Princeton, NJ, USA, ³High Meadows Environmental Institute, Princeton University, Princeton, NJ, USA

Abstract We present a new computational fluid dynamics approach for simulating two-phase flow in hybrid systems containing solid-free regions and deformable porous matrices. Our approach is based on the derivation of a unique set of volume-averaged partial differential equations that asymptotically approach the Navier-Stokes Volume-of-Fluid equations in solid-free regions and multiphase Biot Theory in porous regions. The resulting equations extend our recently developed Darcy-Brinkman-Biot framework to multiphase flow. Through careful consideration of interfacial dynamics (relative permeability and capillary effects) and extensive benchmarking, we show that the resulting model accurately captures the strong two-way coupling that is often exhibited between multiple fluids and deformable porous media. Thus, it can be used to represent flow-induced material deformation (swelling, compression) and failure (cracking, fracturing). The model's open-source numerical implementation, *hybridBiotInterFoam*, effectively marks the extension of computational fluid mechanics into modeling multiscale multiphase flow in deformable porous systems. The versatility of the solver is illustrated through applications related to material failure in poroelastic coastal barriers and surface deformation due to fluid injection in poro-visco-plastic systems.

Plain Language Summary Knowledge of how fluids flow through porous materials has significant implications for the design and operation of batteries, manufacturing plants, oil rigs, and biomedical devices. Even though scientists have been successful in creating computer models that capture fluid flow through *rigid* porous media, it has been very challenging to create models that can model flow through *deformable* porous media. In this study, we describe a new model that can predict flow of immiscible fluids (say water and air, or oil and water) through and around deformable porous media. We derived this model by combining separate conventional fluid-flow and solid-deformation models into a single simulation framework through a technique called volume averaging. The resulting model can capture complex multiscale, multiphysics phenomena such as hydraulic fracturing in the subsurface and its impacts on surface deformation. Given the model's generality, successful verification, and open-source implementation, we are confident that this computational model can be used to study important phenomena in the fields of water and energy resources.

1. Introduction

Multiphase flow in deformable porous media is a ubiquitous phenomenon with important implications in many energy and environmental technologies including geologic CO₂ sequestration, soil bioremediation, water treatment, enhanced biochemical production, nuclear waste disposal, and battery technology (Bächer & Gekle, 2019; Bock et al., 2010; Cunningham et al., 2003; Räss et al., 2018; Towner, 1987). It also underlies iconic geophysical features at many scales, from coastal, riparian, and volcanic landforms to fractures in subsurface reservoirs, cracks in clay soils, and bubbles in soft sediments. An important and largely unresolved challenge in the areas outlined above is the difficulty of describing the inherently multiscale and multiphysics nature of situations where a mixture of several fluids interacts with a deformable porous material. For example, when modeling flow through biofilms or membranes, it is imperative to understand how fluid flow behaves inside the porous medium (in pores with length scales of $\sim 10^{-6}$ m) while simultaneously understanding how the deformation of this medium affects the overall flow field (often controlled by much

© 2020. The Authors.

This is an open access article under the terms of the Creative Commons Attribution License, which permits use, distribution and reproduction in any medium, provided the original work is properly cited.

larger flow paths with length scales on the order of $\sim 10^{-2}$ m) (Bottero et al., 2010). Similarly, the propagation of flow-driven fractures in porous materials and the propagation of waves in coastal barriers involve feedbacks between flow and mechanics in porous and solid-free domains. In the present study, we develop a framework capable of representing multiphase flow through and around deformable porous systems, as required to simulate many of the aforementioned phenomena.

The starting point for our study is based on the present ample understanding of multiphase flow dynamics within and around *static* porous materials, from viscous and capillary fingering (Ferer et al., 2004; Lenormand & Zarcone, 1989; Lenormand et al., 1988) to temperature and surface tension driven flows (Shih & Megaridis, 1996), all the way to turbulent multiphase flows (Colombo & Fairweather, 2015; Soulaine & Quintard, 2014). This knowledge, in conjunction with numerical techniques such as the Lattice Boltzmann Method, the Finite Volume Method, Homogenization Theory, and Averaging Theory, forms the basis of fast and accurate models that are routinely applied to help design and improve hydrocarbon production (Burruis et al., 1991; Mehmani & Tchelepi, 2019), CO₂ sequestration (Hassan & Jiang, 2012), and even nuclear reactors (Tentner et al., 2008). However, the study of multiphase flow across different scales remains limited as shown by the absence of well-established approaches to describe how bubbles or waves propagate into an unsaturated porous medium or how a multiphase fluid mixture is pushed out of a porous medium into open space. Improved understanding of such processes would have a direct and immediate impact in the design of batteries, coastal barriers, natural gas extraction from shales, biochemical gas production, and many other areas.

A similar situation pertains with regard to the coupling between fluid flow and solid mechanics. Theoretical and numerical approaches based on Biot's Theory of poroelasticity (Biot, 1941), Terzaghi's effective stress principle (Terzaghi, 1943), and Mixture Theory (Siddique et al., 2017) have been successful at modeling systems with flow in deformable porous media including arteries, biofilms, boreholes, hydrocarbon reservoirs, seismic systems, membranes, soils, swelling clays, and fractures (Auton & MacMinn, 2017; Barry et al., 1997; Jha & Juanes, 2014; Lo et al., 2002, 2005; MacMinn et al., 2016; Mathias et al., 2017; Santillán et al., 2017). However, as mentioned above, we still have very little understanding of how flow-induced deformation of these solid materials affects the macroscopic flow around them (and thus their boundary conditions) or how fluid-fluid interfaces behave when pushed against a soft porous medium and vice versa. These type of systems are particularly challenging to model because of the multiscale nature of the governing physics, where the curvature of a particular interface and the magnitude of the capillary and/or viscous forces can differ by several orders of magnitude depending on the presence or absence of a porous solid.

Three major approaches have been proposed to resolve the challenge posed by fluid flow in porous media containing both solid-free regions and porous domains (hereafter referred to as multiscale systems). The most straightforward of these involves performing direct numerical simulations (DNS) throughout the entire multiscale domain, both within and outside the porous medium (Breugem & Boersma, 2005; Hahn et al., 2002; Krafczyk et al., 2015). Although rigorous, this technique is impractical in situations with a large difference in length scales between the largest and smallest pores, where it requires exceedingly fine grids and tremendous computational resources.

To save time and resources, other studies have relied on hybrid DNS-Darcy approaches, where fluid and solid mechanics within a porous medium are modeled as averaged quantities through Darcy's law, pore-network models, or Biot's theory of poroelasticity (Ehrhardt, 2010; Weishaupt et al., 2019). One such approach relies on the use of the Beavers-Joseph (BJ) boundary condition to couple fluid flow in solid-free domains (simulated using the Navier-Stokes Equations) and in porous domains (simulated using Darcy's law) for *single* phase flow and *static* porous media (Beavers & Joseph, 1967; Fetzer et al., 2016). Recent studies have extended this BJ approach to allow multiphase flow in the solid-free domain (Baber et al., 2016) or to include the effects of poroelasticity within the porous medium (Lacis et al., 2017; Zampogna et al., 2019). However, to the best of our knowledge, no BJ-based technique has yet been developed to couple solid mechanics with multiphase flow simultaneously within the solid-free and porous domains.

The Darcy-Brinkman (DB) approach presents a well-known alternative to the BJ interface matching technique. The crux of the DB approach is the use of a spatially dependent penalization term within the Navier-Stokes fluid momentum equation. This term effectively creates an equation that approximates

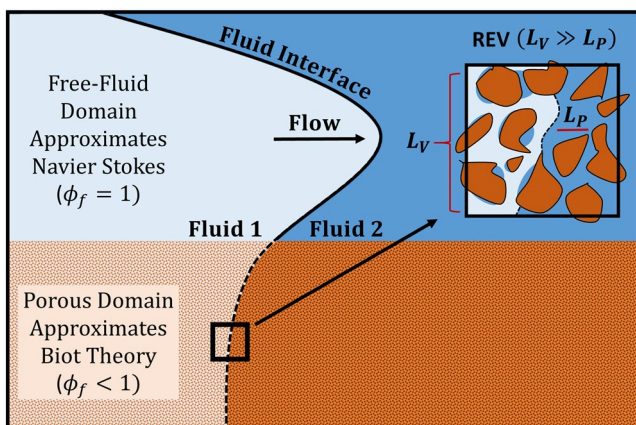


Figure 1. Conceptual representation of the multiphase Darcy-Brinkman-Biot model. The inset represents an exemplary Representative Elementary Volume (REV) within the porous domain and ϕ_f is the porosity. The model considers wetting properties, interface mechanics, and irreducible saturations when averaging over a REV. Note that the stated relation between the averaging volume's length scale L_V and the porous length scale L_P is required for the creation of a REV, and thus, for the application of this model.

Navier-Stokes within solid-free domains and Darcy's law within porous domains. Although initially implemented as an empirical approach (Brinkman, 1947), this technique has since been formalized and rigorously derived from first principles through volume averaging theory (Soulaine et al., 2016; Whitaker, 2013). The resulting so-called "microcontinuum" approach has been extensively used to solve *single* phase flow through *static* multiscale porous media, such as flow in biofilms (Kapellos et al., 2007) and in rocks containing unresolved porosity (Guo et al., 2018; Kang et al., 2019; Singh, 2019). The approach has proved highly flexible as illustrated by its uses to represent embedded solid boundaries in low-permeability media (Khadra et al., 2000) and the evolution of solid grain morphologies caused by mineral dissolution (Soulaine et al., 2017, 2019).

Recently, a study by Carrillo and Bourg (2019) introduced a Darcy-Brinkman-Biot (DBB) approach capable of accurately representing *single* phase flow in multiscale *deformable* media including elastic porous membranes and plastic swelling clays. Simultaneously, studies by Soulaine et al. (2019) and Carrillo et al. (2020) extensively benchmarked and released an open-source extension of the microcontinuum framework for *multiphase* flow in *static* multiscale porous media. This allowed accurate modeling of complex systems such as multiphase flow in a fractured porous medium, methane extraction from tight porous media, and wave absorption in coastal barriers. In the present paper, we build upon these previous studies to create the first model representing coupled fluid and solid mechanics during *multiphase* flow in *multiphase* porous media: the multiphase DBB model (Figure 1).

This study is organized as follows. Section 2 introduces the concept of volume averaging and describes the derivation of the governing equations for coupled fluid and solid mechanics. Section 3 explains the numerical implementation and algorithm development for the coupled mass and momentum equations and introduces the resulting open-source solver "*hybridBiotInterFoam*." Section 4 presents five test cases that verify the implementation of different coupling terms within the model, with an emphasis on fracturing mechanics. Section 5 then presents two alternative applications that illustrate the versatility of the model: wave absorption in poroelastic coastal barriers and surface deformation due to fluid injection in poro-visco-plastic geologic formations. Lastly, Section 6 concludes with a summary of the paper and a discussion on future work.

2. Model Derivation

2.1. Volume Averaging

In this section, we introduce the concept of volume averaging. This technique forms the basis of the microcontinuum equations, as it allows the classical mass and momentum conservation equations to account for the coexistence of solid (s), wetting fluid (w), and nonwetting fluid (n) within a given control volume. It is well suited for use in conjunction with the Finite Volume Method (FVM) (Patankar, 1980), as the numerical grid elements used in the FVM provide an intuitive and straightforward numerical interpretation of what we will define as the averaging volume (V). In keeping with standard volume averaging theory, we start by defining the volume averaging operator

$$\bar{\beta}_i = \frac{1}{V} \int_{V_i} \beta_i dV \quad (1)$$

where β_i is a function defined in each phase's respective volume V_i ($i = w, n, s$), and $V = \text{sum}(V_i)$. We also define the phase averaging operator

$$\bar{\beta}_i^i = \frac{1}{V_i} \int_{V_i} \beta_i dV \quad (2)$$

The volume and phase-averaged variables associated with the fluids are intrinsically related by the porosity ($\phi_f = (V_w + V_n)/V$) and saturation fields ($\alpha_i = V_i/(V_w + V_n)$), such that $\bar{\beta}_i = \phi_f \alpha_i \bar{\beta}_i^i$ ($i = w, n$). For solid variables, the analogous relation involves only the solid fraction ϕ_s , such that $\bar{\beta}_s = \phi_s \bar{\beta}_s^s$. Note that $\phi_f + \phi_s = 1$ and $\alpha_w + \alpha_n = 1$; thus, knowledge of one of the ϕ_i or α_i variables implies knowledge of the other. Volume averaging then allows for the definition of several regions within a multiscale, multiphase system such as that represented in Figure 1:

$$\phi_f = \begin{cases} 1, & \text{in solid - free regions} \\ 0;1, & \text{in porous regions} \end{cases} \quad (3)$$

$$\alpha_w = \begin{cases} 0, & \text{in regions saturated with non wetting fluid} \\ 0;1, & \text{in unsaturated regions} \\ 1, & \text{in regions saturated with wetting fluid} \end{cases} \quad (4)$$

The application of an averaging transformation to fluid and solid conservation equations will result in variables and equations that are weighted differently in each region. However, the averaging of differential equations is not straightforward, which is why we introduce the following spatial averaging theorems for volumes containing three distinct phases (Howes & Whitaker, 1985; Whitaker, 1999)

$$\overline{\frac{\partial \beta_i}{\partial t}} = \frac{\partial \bar{\beta}_i}{\partial t} - \frac{1}{V} \int_{A_{i,j}} \beta_i \mathbf{v}_{i,j} \cdot \mathbf{n}_{i,j} dA - \frac{1}{V} \int_{A_{i,k}} \beta_i \mathbf{v}_{i,k} \cdot \mathbf{n}_{i,k} dA \quad (5)$$

$$\overline{\nabla \beta_i} = \nabla \bar{\beta}_i + \frac{1}{V} \int_{A_{i,j}} \beta_i \mathbf{n}_{i,j} dA + \frac{1}{V} \int_{A_{i,k}} \beta_i \mathbf{n}_{i,k} dA \quad (6)$$

$$\overline{\nabla \cdot \beta_i} = \nabla \cdot \bar{\beta}_i + \frac{1}{V} \int_{A_{i,j}} \beta_i \cdot \mathbf{n}_{i,j} dA + \frac{1}{V} \int_{A_{i,k}} \beta_i \cdot \mathbf{n}_{i,k} dA \quad (7)$$

where $A_{i,j}$ represents the interfacial area between phase i and j , $\mathbf{n}_{i,j}$ is a vector normal to the interface and oriented toward phase j , and $\mathbf{v}_{i,j}$ is the velocity of the interface. The notation for symbols with subscript pair i, k is equivalent. Note that the symbols i, j, k represent any combination of the solid, wetting, and nonwetting phases. These surface integrals are crucial components of the following derivations as they convert the interfacial conditions at the fluid-fluid and fluid-solid interfaces into body forces within the averaged partial differential equations.

2.2. Derivation of the Fluid Mechanics Equations

We begin the derivation by stating the microcontinuum equations for two immiscible incompressible fluids, which arise from applying the volume averaging operators (Equations 5–7) to the classical Navier-Stokes conservation equations for both a wetting and a nonwetting fluid, and, then, adding together each pair of averaged mass and momentum equations through the definition of “single-field” variables (i.e., averaged variables that depend on the properties of both fluids). This set of equations can also be thought of as a modified and expanded version of the popular Volume-of-Fluid equations (Hirt & Nichols, 1981). A detailed derivation of the following expressions can be found in Carrillo et al. (2020).

$$\frac{\partial \phi_f}{\partial t} + \nabla \cdot \mathbf{U}_f = 0 \quad (8)$$

$$\frac{\partial \phi_f \alpha_w}{\partial t} + \nabla \cdot (\alpha_w \mathbf{U}_f) + \nabla \cdot (\phi_f \alpha_w \alpha_n \mathbf{U}_r) = 0 \quad (9)$$

$$\frac{\partial \rho_f \mathbf{U}_f}{\partial t} + \nabla \cdot \left(\frac{\rho_f}{\phi_f} \mathbf{U}_f \mathbf{U}_f \right) = -\phi_f \nabla p + \phi_f \rho_f \mathbf{g} + \nabla \cdot \bar{\mathbf{S}} \\ + \mathbf{D}_{w,s} + \mathbf{D}_{n,s} + \mathbf{D}_{s,w} + \mathbf{D}_{s,n} + \mathbf{D}_{w,n} + \mathbf{D}_{n,w} \quad (10)$$

where the $\mathbf{D}_{i,k} = \frac{1}{V} \int_{A_{i,k}} \mathbf{n}_{i,k} \cdot (-I p_i + \mathbf{S}_i) dA$ vectors represent the momentum exchange from phase i to phase k ($i, k = w, n, s$) as a direct result of volume averaging. Additionally, $\bar{\mathbf{S}} = \mu_f (\nabla \mathbf{U}_f + (\nabla \mathbf{U}_f)^T)$ is the averaged single-field viscous stress tensor, \mathbf{g} is gravity, μ_f is the volume-weighted average of each fluid's viscosity $\mu_f = \alpha_w \mu_w + \alpha_n \mu_n$, and ρ_f is the volume-weighted average of each fluid's density $\rho_f = \alpha_w \rho_w + \alpha_n \rho_n$. The single-field expressions for velocity \mathbf{U}_f , pressure p , and relative velocity \mathbf{U}_r are defined as the weighted averages of their respective phase-averaged variables.

$$\mathbf{U}_f = \phi_f \left[\alpha_w \bar{\mathbf{U}}_w^w + \alpha_n \bar{\mathbf{U}}_n^n \right] \quad (11)$$

$$p = \alpha_w \bar{p}_w^w + \alpha_n \bar{p}_n^n \quad (12)$$

$$\mathbf{U}_r = \bar{\mathbf{U}}_w^w - \bar{\mathbf{U}}_n^n \quad (13)$$

We note that the single-phase velocity as defined above is equal to the sum of the volume-averaged velocities: $\mathbf{U}_f = \bar{\mathbf{U}}_w + \bar{\mathbf{U}}_n$. As described in Carrillo and Bourg (2019) and Carrillo et al. (2020), these terms can be recast into the following expression through asymptotic matching to the standard multiphase Darcy equations:

$$\frac{\partial \rho_f \mathbf{U}_f}{\partial t} + \nabla \cdot \left(\frac{\rho_f}{\phi_f} \mathbf{U}_f \mathbf{U}_f \right) = -\phi_f \nabla p + \phi_f \rho_f \mathbf{g} + \nabla \cdot \bar{\mathbf{S}} \\ - \phi_f \mu k^{-1} (\mathbf{U}_f - \bar{\mathbf{U}}_s) + \phi_f \mathbf{F}_{c,1} + \phi_f \mathbf{F}_{c,2} \quad (14)$$

where μk^{-1} is the drag coefficient (a function of the fluid viscosities and permeability k), $\bar{\mathbf{U}}_s$ is the averaged solid velocity, $\phi_f \mu k^{-1} (\mathbf{U}_f - \bar{\mathbf{U}}_s)$ is a solid-fluid momentum exchange term that accounts for a moving porous medium in an Eulerian frame of reference, and $\mathbf{F}_{c,i}$ represents the forces emanating from fluid-fluid and fluid-solid capillary interactions. As shown in Carrillo et al. (2020),

$$\mathbf{F}_{c,1} = \begin{cases} -\frac{\gamma}{\phi_f} \nabla \cdot (\mathbf{n}_{w,n}) \nabla \alpha_w & \text{in solid - free regions} \\ -p_c \nabla \alpha_w & \text{in porous regions} \end{cases} \quad (15)$$

$$\mathbf{F}_{c,2} = \begin{cases} 0 & \text{in solid - free regions} \\ M^{-1} (M_w \alpha_n - M_n \alpha_w) (\nabla p_c + (\rho_w - \rho_n) \mathbf{g}) & \text{in porous regions} \end{cases} \quad (16)$$

where p_c is the average capillary pressure within a given averaging volume, γ is the fluid-fluid interfacial tension, $M_i = k_0 k_{i,r} / \mu_i$ is the mobility of each fluid (a function of absolute permeability k_0 and relative permeability $k_{i,r}$), and $M = M_w + M_n$ is the single-field fluid mobility. Lastly, $\mathbf{n}_{w,n}$ is the unit normal direction of the fluid-fluid interface as calculated by the Continuum Surface Force (CSF) formulation (Brackbill et al., 1992). The equations presented above tend toward the standard Navier-Stokes Volume-of-Fluid approach in solid-free regions (where the drag term becomes negligible) and toward the multiphase Darcy equations in porous regions. The latter can be explained by the fact that the viscous stress tensor $\nabla \cdot \bar{\mathbf{S}}$ becomes negligible under the scale-separation assumption, inertial terms become negligible under the assumption of low

Reynold's number flow in the porous medium, and the \mathbf{F}_c , terms are set to fit standard multiphase Darcy's law (Carrillo et al., 2020; Whitaker, 1986):

$$\text{Eqn. 14} \approx \begin{cases} \frac{\partial \rho_f \mathbf{U}_f}{\partial t} + \nabla \cdot (\rho_f \mathbf{U}_f \mathbf{U}_f) = -\nabla p + \nabla \cdot \bar{\mathbf{S}} + \rho_f \mathbf{g} + \mathbf{F}_{c,1} & \text{in solid - free regions} \\ (\mathbf{U}_f - \bar{\mathbf{U}}_s) = -\frac{k}{\mu}(\nabla p - \rho_f \mathbf{g} - \mathbf{F}_{c,1} - \mathbf{F}_{c,2}) & \text{in porous regions} \end{cases} \quad (17)$$

2.3. Derivation of the Solid Mechanics Equations

We proceed with the derivation of the microcontinuum solid mechanics equations by starting from the equations presented in Carrillo and Bourg (2019) for solid mass and momentum conservation in systems with a single incompressible solid phase.

$$\frac{\partial \phi_s}{\partial t} + \nabla \cdot (\phi_s \bar{\mathbf{U}}_s^s) = 0 \quad (18)$$

$$-\nabla \cdot \bar{\boldsymbol{\sigma}} = \phi_s \nabla \cdot \bar{\boldsymbol{\tau}}^s + \phi_s \rho_s \mathbf{g} + \mathbf{B}_{s,w} + \mathbf{B}_{s,n} \quad (19)$$

where $\bar{\boldsymbol{\sigma}}$ is the volume-averaged solid elastic (or plastic) stress tensor and $\bar{\boldsymbol{\tau}}^s = \mathbf{P}_{\text{conf}} - \mathbf{I}p - \mathbf{I}p_{\text{swell}}$ is the Terzaghi effective stress tensor (a function of confining pressure \mathbf{P}_{conf} , fluid pressure p , and swelling or disjoining pressure p_{swell}). Here, the $\mathbf{B}_{s,i} = \frac{1}{V} \int_{A_{s,i}} (\boldsymbol{\tau} + \boldsymbol{\sigma}) \cdot \mathbf{n}_{s,i} dA$ values represent the momentum exchange between the solid phase s and fluid phase i ($i = w, n$). Just as we did for the fluid equations, we will assume that the sum of the averaged stresses at the solid-fluid interface can be expressed as the sum of two independent terms: a drag force that captures shear-induced momentum exchange (\mathbf{B}_{drag}) and a capillary force originating from capillary pressure jumps across the integrated solid surfaces within the porous media (\mathbf{B}_{cap}).

$$\mathbf{B}_{s,w} + \mathbf{B}_{s,n} = \mathbf{B}_{\text{drag}} + \mathbf{B}_{\text{cap}} \quad (20)$$

We now seek closure of these two coupling terms. By conservation of momentum, we know that any drag-induced momentum lost by the fluid must be gained by the solid. Therefore, we can use the drag term used in Equation 14 to obtain (Carrillo & Bourg, 2019)

$$\mathbf{B}_{\text{drag}} = \phi_f \mu k^{-1} (\mathbf{U}_f - \bar{\mathbf{U}}_s) \quad (21)$$

Closure of the capillarity-induced interaction term \mathbf{B}_{cap} is obtained by combining the solid and fluid momentum equations within the porous medium at low Reynold numbers and low permeability, which yields

$$-\nabla \cdot \bar{\boldsymbol{\sigma}} = \phi_s \nabla \cdot \bar{\boldsymbol{\tau}}^s - \phi_f \nabla p + (\phi_s \rho_s + \phi_f \rho_f) \mathbf{g} + \phi_f \mathbf{F}_{c,1} + \phi_f \mathbf{F}_{c,2} + \mathbf{B}_{\text{cap}} \quad (22)$$

In multiphase porous systems with incompressible grains and no swelling pressure (i.e., $\nabla \cdot \bar{\boldsymbol{\tau}}^s = -\nabla p$), Biot Theory states that $\nabla \cdot \bar{\boldsymbol{\sigma}} = \nabla p - \rho^* \mathbf{g} + p_c \nabla \alpha_w$, where $\rho^* = (\phi_s \rho_s + \phi_f \rho_f)$ and p_c is the capillary pressure (Jha & Juanes, 2014; Kim et al., 2013). This expression is satisfied by the previous equation in the absence of capillary forces, where $\mathbf{F}_{c,1}$, $\mathbf{F}_{c,2}$, \mathbf{B}_{cap} , and p_c equal zero (Carrillo & Bourg, 2019). In the presence of capillary forces, however, it imposes the following equality

$$\mathbf{B}_{\text{cap}} = -(\phi_f \mathbf{F}_{c,1} + \phi_f \mathbf{F}_{c,2} + p_c \nabla \alpha_w) \quad (23)$$

Given that $\mathbf{F}_{c,1} = -p_c \nabla \alpha_w$ in the porous domains (Carrillo et al., 2020), the previous equation can be rearranged to obtain

$$\mathbf{B}_{\text{cap}} = \phi_s \mathbf{F}_{c,1} - \phi_f \mathbf{F}_{c,2} \quad (24)$$

Equation 24 gives closure to the last coupling parameter and marks the end of this derivation. The result is a solid conservation equation that tends toward Biot Theory in porous regions and toward an infinitely deformable solid with no momentum sources in solid-free regions.

2.4. Interfacial Conditions Between Solid-Free Regions and Porous Regions

One of the most important features within the framework presented above is the existence of an interface between solid-free and porous domains. Although the creation of a rigorous unaveraged description of this interface is still an open question, we approximate a solution to it by guaranteeing its necessary components within our fluid and solid averaged equations.

An accurate description of fluid behavior at the interface requires three components: (1) mass conservation across the interface, (2) continuity of stresses across the interface, and (3) an interfacial wettability condition. Components 1 and 2 are intrinsically fulfilled by our solver due to its single-field formulation for velocity and pressure within the fluid conservation equations (Equations 8 and 14). As shown in Neale and Nader (1974) and Carrillo and Bourg (2019), these two components are necessary and sufficient to model single-phase flow within a multiscale system. Furthermore, these conditions have also been used for closure when modeling multiphase flow in moving porous media (Carrillo et al., 2020; Lacis et al., 2017; Zampogna et al., 2019). The required wettability condition at the porous interface (Component 3) is included in our model through the implementation of a penalized contact angle condition (Equation 33) following the steps outlined in Horgue et al. (2014) and Carrillo et al. (2020).

The complementary solid conditions at the porous interface are very similar: (1) solid mass conservation across the interface, (2) continuity of fluid-induced stresses across the interface, and (3) a discontinuity of solid stresses at the interface. Just as before, the first two conditions are intrinsically fulfilled through the use of a single set of mass and momentum conservation equations across both domains and have also been used as closure conditions in previous studies (Lacis et al., 2017; Zampogna et al., 2019). The third condition is enforced by the use of volume-averaged solid rheology models that tend toward infinitely deformable materials in solid-free regions, as shown in Carrillo and Bourg (2019). When volume-averaged, the behavior of the solid's stress tensor is domain dependent (i.e., solid fraction dependent). Thus, in solid regions, the elasticity and viscosity of the porous medium is determined by standard averaged rheological properties (the elastic and viscoplastic moduli). Contrastingly, in solid-free regions, the solid fraction tends to zero and, as such, said properties do as well. The result is a stress-free “ghost” solid that does not apply resistance to the porous region, creating the required stress discontinuity at the porous interface.

Although necessary, these conditions represent but an approximation to the complete description of fluid and solid mechanics at the porous interface. However, to the best of our knowledge, there does not exist an alternative set of interfacial conditions that can or have been used to model multiphase flow in multiscale porous media.

2.5. Model Summary

The final set of equations in our proposed multiphase DBB framework now follows. The combination of these solid and fluid conservation equations leads to a model that tends toward multiphase Navier-Stokes in solid-free regions and toward Biot Theory in porous regions, as described in Figure 1.

$$\frac{\partial \phi_f}{\partial t} + \nabla \cdot \mathbf{U}_f = 0 \quad (25)$$

$$\frac{\partial \phi_f \alpha_w}{\partial t} + \nabla \cdot (\alpha_w \mathbf{U}_f) + \nabla \cdot (\phi_f \alpha_w \alpha_n \mathbf{U}_r) = 0 \quad (26)$$

$$\frac{\partial \rho_f \mathbf{U}_f}{\partial t} + \nabla \cdot \left(\frac{\rho_f}{\phi_f} \mathbf{U}_f \mathbf{U}_f \right) = -\phi_f \nabla p + \phi_f \rho_f \mathbf{g} + \nabla \cdot \bar{\mathbf{S}} \\ -\phi_f \mu k^{-1} (\mathbf{U}_f - \bar{\mathbf{U}}_s) + \phi_f \mathbf{F}_{c,1} + \phi_f \mathbf{F}_{c,2} \quad (27)$$

$$\frac{\partial \phi_s}{\partial t} + \nabla \cdot (\phi_s \bar{\mathbf{U}}_s) = 0 \quad (28)$$

$$-\nabla \cdot \bar{\boldsymbol{\sigma}} = \phi_s \nabla \cdot \bar{\boldsymbol{\tau}}^s + \phi_s \rho_s \mathbf{g} + \phi_f \mu k^{-1} (\mathbf{U}_f - \bar{\mathbf{U}}_s) - \phi_f \mathbf{F}_{c,1} + \phi_s \mathbf{F}_{c,2} \quad (29)$$

All that is left is stating the closed-form expressions of the multiscale parameters μk^{-1} , $\mathbf{F}_{c,i}$, and \mathbf{U}_r , which are defined differently in each region. A full derivation and discussion of these parameters can be found in Carrillo et al. (2020).

$$\mu k^{-1} = \begin{cases} 0 & \text{in solid - free regions} \\ k_0^{-1} \left(\frac{k_{r,w}}{\mu_w} + \frac{k_{r,n}}{\mu_n} \right)^{-1} & \text{in porous regions} \end{cases} \quad (30)$$

$$\mathbf{F}_{c,1} = \begin{cases} -\frac{\gamma}{\phi_f} \nabla \cdot (\mathbf{n}_{w,n}) \nabla \alpha_w & \text{in solid - free regions} \\ -p_c \nabla \alpha_w & \text{in porous regions} \end{cases} \quad (31)$$

$$\mathbf{F}_{c,2} = \begin{cases} 0 & \text{in solid - free regions} \\ M^{-1} (M_w \alpha_n - M_n \alpha_w) (\nabla p_c + (\rho_w - \rho_n) \mathbf{g}) & \text{in porous regions} \end{cases} \quad (32)$$

$$\mathbf{n}_{w,n} = \begin{cases} \frac{\nabla \alpha_w}{|\nabla \alpha_w|} & \text{in solid - free regions} \\ \cos(\theta) \mathbf{n}_{wall} + \sin(\theta) \mathbf{t}_{wall} & \text{at the interface between solid - free porous regions} \end{cases} \quad (33)$$

$$\mathbf{U}_r = \begin{cases} C_\alpha \max(|\mathbf{U}_f|) \frac{\nabla \alpha_w}{|\nabla \alpha_w|} & \text{in solid - free regions} \\ \phi_f^{-1} \left[\begin{array}{l} - (M_w \alpha_w^{-1} - M_n \alpha_n^{-1}) \nabla p + \\ (\rho_w M_w \alpha_w^{-1} - \rho_n M_n \alpha_n^{-1}) \mathbf{g} + \\ (M_w \alpha_n \alpha_w^{-1} + M_n \alpha_w \alpha_n^{-1}) \nabla p_c - \\ (M_w \alpha_w^{-1} - M_n \alpha_n^{-1}) p_c \nabla \alpha_w \end{array} \right] & \text{in porous regions} \end{cases} \quad (34)$$

where C_α is an interface compression parameter (traditionally set to values between 1 and 4 in the Volume-of-Fluid method), k_0 is the absolute permeability, $k_{r,i}$ and $M_i = k_0 k_{i,r} / \mu_i$ are the relative permeability and mobility of each fluid, and $M = M_w + M_n$. Lastly, θ is the imposed contact angle at the porous wall, and \mathbf{n}_{wall} and \mathbf{t}_{wall} are the normal and tangential directions relative to said wall, respectively.

Finally, closure of the system of equations requires appropriate constitutive models describing the averaged behavior of the different phases within the porous regions. For the purpose of validating our multiphase

DBB approach, in the present study, we use the following well-established constitutive models: absolute permeability is modeled as isotropic and porosity-dependent through the well-known Kozeny-Carman relation $k_0 = k_0^0 \frac{\phi_f^3}{(1 - \phi_f)^2}$; relative permeabilities and average capillary pressures within the porous domains are represented using the Van Genuchten (van Genuchten, 1980) and Brooks-Corey (Brooks & Corey, 1964) models (Appendix A); plasticity is described through the Herschel-Bulkley model, were the solid viscously deforms only after local stresses become higher than the material yield stress (Appendix B1); the solid's yield stress and plastic viscosity are modeled as solid fraction-dependent based on the Quemada fractal model (Quemada, 1977; Spearman, 2017) (Appendix B2); finally, elastic solids are modeled as averaged linear-elastic materials, such that their averaged elastic coefficients scale linearly with respect to the solid fraction (Appendix B3). The last three choices imply that solid rheological properties are modeled as isotropic and independent of saturation, a significant simplification that is sufficient for the purpose of testing and validating the present framework. For the reader's convenience, a full implementation of this framework and its related models are included in the accompanying simulation "toolbox." If necessary, more complex constitutive models, such as the saturation-depended solid rheology models presented in Wan et al. (2014), Oldecop and Alonso (2003), Buscarnera and Einav (2012), and Di Donato et al. (2003) can be readily implemented into our code by virtue of its open-source implementation.

3. Numerical Implementation

3.1. Numerical Platform

The implementation of the multiphase DBB model was done in OpenFOAM®, a free, open-source, parallelizable, and widely used computational fluid mechanics platform. This C++ code uses the Finite Volume Method to discretize and solve partial differential equations in complex 3-D grids. Its object-oriented structure and multitude of supporting libraries allows the user to easily customize each simulation's setup with different numerical discretization schemes, time-stepping procedures, matrix-solution algorithms, and supporting physical models. The implementation described below represents the natural extension of the multiphase microcontinuum toolkit "*hybridInterFoam*" (Carrillo et al., 2020) to systems with deformable solids. In particular, its solution algorithm stems directly from that used by "*hybridInterFoam*" and its precursor "*interFoam*."

3.2. Solution Algorithm

The solution of the governing equations is done in a sequential manner, starting with the fluid mechanics equations and following with the solid mechanics equations for every time step. Of particular importance is the handling and modification of the velocity-pressure coupling required for modeling incompressible fluids in conjunction with a moving solid matrix. For this step, we based our solution algorithm on the Pressure Implicit Splitting-Operator (Issa, 1986). First, we explicitly solve the fluid saturation equation (Equation 9) for α_w^{t+1} through the Multidimensional Universal Limiter of Explicit Solution algorithm (Márquez & Fich, 2013). This allows for stable numerical advection of the saturation field by the application of Flux Corrected Transport Theory (Rudman, 1997). Then, we update the boundary values of \mathbf{U}_f and \mathbf{U}_r in addition to the cell-centered values of the permeability k^{t+1} , density ρ_f^{t+1} , and viscosity μ_f^{t+1} based on the newly calculated saturation field α_w^{t+1} . The capillary forces $\mathbf{F}_{c,i}^{t+1}$ are also updated accordingly. After that, a preliminary value of the fluid velocity \mathbf{U}_f^* is calculated by implicitly solving the algebraically discretized form of the fluid momentum equation used in the Finite Volume Method.

$$a_p \mathbf{U}_f^* = \mathbf{H}(\mathbf{U}_f^*) + \rho_f^{t+1} \mathbf{g} + \mathbf{F}_{c,i}^{t+1} - \nabla p^t \quad (35)$$

where $\mathbf{H}(\mathbf{U}_f^*)$ contains inertial, convective, viscous, and drag source terms originating from neighboring cells and a_p represents these same terms but at the volume of interest. Note that the \mathbf{U}_f^* field does not follow

mass conservation. To account for this, we use the fluid continuity equation (Equation 25) in conjunction with the previous equation (Equation 35) to update the velocity field \mathbf{U}_f^{**} and calculate a preliminary mass-conservative pressure field p^* . In other words, these fields must satisfy,

$$\mathbf{U}_f^{**} = \frac{1}{a_p} \left(\mathbf{H}(\mathbf{U}_f^*) + \rho_f^{t+1} \mathbf{g} + \mathbf{F}_{c,i}^{t+1} - \nabla p^* \right) \quad (36)$$

$$\nabla \cdot \mathbf{U}_f^{**} = - \frac{\partial \phi_f}{\partial t} \quad (37)$$

These equations can be recast into a single coupled equation which is then used to implicitly solve for pressure. This step can be done through several generalized matrix solvers that are standard in OpenFOAM®.

$$\nabla \cdot \left(\frac{1}{a_p} \left(\mathbf{H}(\mathbf{U}_f^*) + \rho_f^{t+1} \mathbf{g} + \mathbf{F}_{c,i}^{t+1} \right) \right) - \nabla \cdot \left(\frac{1}{a_p} \nabla p^* \right) = - \frac{\partial \phi_f}{\partial t} \quad (38)$$

After solving for pressure p^* , velocity can be recalculated from Equation 36. This semi-implicit pressure-velocity correction step is repeated until the desired convergence is reached. It has been shown that at least two pressure-velocity correction loops are required to ensure mass conservation (Issa, 1986).

At this point, \mathbf{U}_f^{t+1} and p^{t+1} are set and used as input values for updating the drag and pressure source terms present in the solid mechanics momentum equation (Equation 29). Then, in the case of visco-poro-plasticity, said equation is discretized in a similar way as the fluid momentum equation (Equation 27) and used to implicitly solve for \mathbf{U}_s^{t+1} . In the case of poroelasticity, the solid mechanics equation is solved through the algorithm presented in Jasak and Weller (2000). Here, the solid's elastic equation (Equation 29) is discretized and segregated into implicit and explicit components, after which it is iteratively solved until convergence is reached. This segregated method not only guarantees fast convergence but also memory efficiency. Finally, the updated solid velocity is used to “advect” the solid fraction field ϕ_s by solving the mass conservation equation (Equation 28). At this point, the algorithm advances in time according to the imposed Courant-Friedrichs-Lowy number. A flow-chart of the complete algorithm can be found in the Supporting Information (SI), and further discussion regarding the discretization techniques and matrix-solution procedures can be found in Carrillo et al. (2020), Jasak (1996), and Jasak and Weller (2000).

3.3. Open-Source Implementation

The complete set of governing equations and solution algorithms, along with the necessary rheology, relative permeability, and capillary pressure models (Appendices A and B) were implemented into a single solver: “*hybridBiotInterFoam*.” This solver, along with its representative tutorial cases, automated compilation and running procedures, and all the simulated cases presented in this paper were incorporated into an open-source CFD package of the same name. OpenFOAM® and our code are free to use under the GNU general public license and can be found at <https://openfoam.org/> and <https://github.com/Franjcf> (Carrillo & Bourg, 2020), respectively.

4. Model Validation

Most of the underlying components of the approach described above have been previously tested and verified. Carrillo and Bourg (2019) validated the momentum exchange terms as an effective coupling mechanism between a *single* fluid phase and a *deformable* plastic or elastic porous medium. The effects of confining and swelling pressures on porous media were also examined in said study. Then, Carrillo et al. (2020) extensively validated the extension of the Darcy-Brinkman equation into multiphase flow within and around *static* porous media by comparison with reference test cases in a wide range of flow, permeability, capillarity, and wettability conditions. Therefore, the only thing left to validate is the ability of the multiphase DBB model

to accurately predict the behavior of multiscale systems that exhibit coupling effects between multiple fluids and a deformable porous matrix.

To that point, we begin with two validation cases relating to multiphase poroelasticity and the coupling between solid deformation and fluid pressure. Then, we proceed with two poro-visco-plastic cases that validate this framework for multiscale plastic systems. Finally, we conclude with two additional cases that verify the implementation of the capillary force interaction terms. All of these can be found in the accompanying CFD simulation package. We note that all validation cases presented below were tested for grid-independence. A sample of these tests pertaining to Figures 4–7 can be found in the SI.

4.1. Terzaghi Consolidation Problem

The Terzaghi uniaxial compaction test has been extensively used as a benchmark for the validation of numerical codes relating to poroelasticity (Terzaghi et al., 1996). Its main utility is to test the accuracy of the solid-fluid couplings that relate fluid pressure to solid deformation and *vice versa*. The problem consists of a constrained saturated elastic porous medium that is abruptly compressed from its upper boundary by a constant uniaxial load (Figure 2). This creates a sudden increase in pore pressure, which is then dissipated by flow through the upper boundary (all other boundaries have impermeable boundary conditions). In the case of a one-dimensional porous medium, the resulting temporal and spatial evolution in fluid pressure can be described by the following simplified analytical solution (Verruijt, 2013).

$$\frac{p}{p_{max}} = \operatorname{erf}\left(\frac{h-z}{2\sqrt{c_v t}}\right) \quad \text{for } \frac{c_v t}{h^2} \ll 1 \quad (39)$$

where $c_v = (k_0 E (\nu - 1)) / (\rho_f g (2\nu^2 + \nu - 1))$ is the consolidation coefficient, k_0 is permeability, E is Young's modulus, ν is Poisson's ratio, h is the column height, and z is the vertical coordinate. Our equivalent numerical setup is shown in Figure 2. The values of the relevant parameters in our simulations are $h = 10$ m, $k_0 = 5 \times 10^{-11}$ m², $E = 2$ MPa, and $\nu = 0.25$. To show the accuracy of our model across different conditions, the loading pressure was varied from 10 to 200 kPa (Figure 2b) and the porosity from 0.25 to 0.75 (Figure 2c). Lastly, the column was partially saturated ($\alpha_w = 0.5$) with fluids with equal densities ($\rho_f = 1,000$ kg/m³), viscosities ($\mu_f = 1$ cp), and negligible capillary effects. This last point allowed for testing the validity of the fluid-solid couplings irrespective of the simulated phases without violating any of the assumptions present in the analytical solution. Our numerical results show excellent agreement with Equation 39 for all tested conditions. Further verification of these terms for an oscillating linear-elastic solid with pressure boundary conditions (as opposed to stress boundary conditions) can be found in the SI.

4.2. Capillary Pressure Effects in a Poroelastic Column

Having verified the two-way coupling between solid deformation and fluid pressure, we now verify the implementation of the capillary pressure terms within the solid mechanics equation. To do so, we simulate a poroelastic column (1 m tall, 1,500 Cells, $\phi_f = 0.5$) bounded by two nonwetting fluid reservoirs at its upper and lower boundaries. The column is initialized with a linear saturation profile spanning from $\alpha_w = 0$ to 1 (see Figure 3). Fluid saturation is kept fixed by not solving Equation 26, and the mobilities of both fluids are set to very high values ($M_i = 1 \times 10^{10}$ m³/kg.s) to minimize drag-related effects. Under these conditions, the solid's effective vertical stress is exclusively controlled by capillary effects and is described by the following analytical solution:

$$\sigma_{\text{vertical}} = \phi_s \alpha_w p_c \quad (40)$$

We used the Van Genutchen capillary pressure model with $m = 0.6$ or 0.8 and $p_{c,0} = 50$ –2,000 Pa to calculate the solutions to said problem. The resulting agreement between the numerical and analytical solutions, shown in Figure 3, confirms the accuracy of the fluid-solid capillary pressure coupling implemented in our model. Furthermore, the transitional behavior of the effective stress at the macroscopic solid-fluid interface

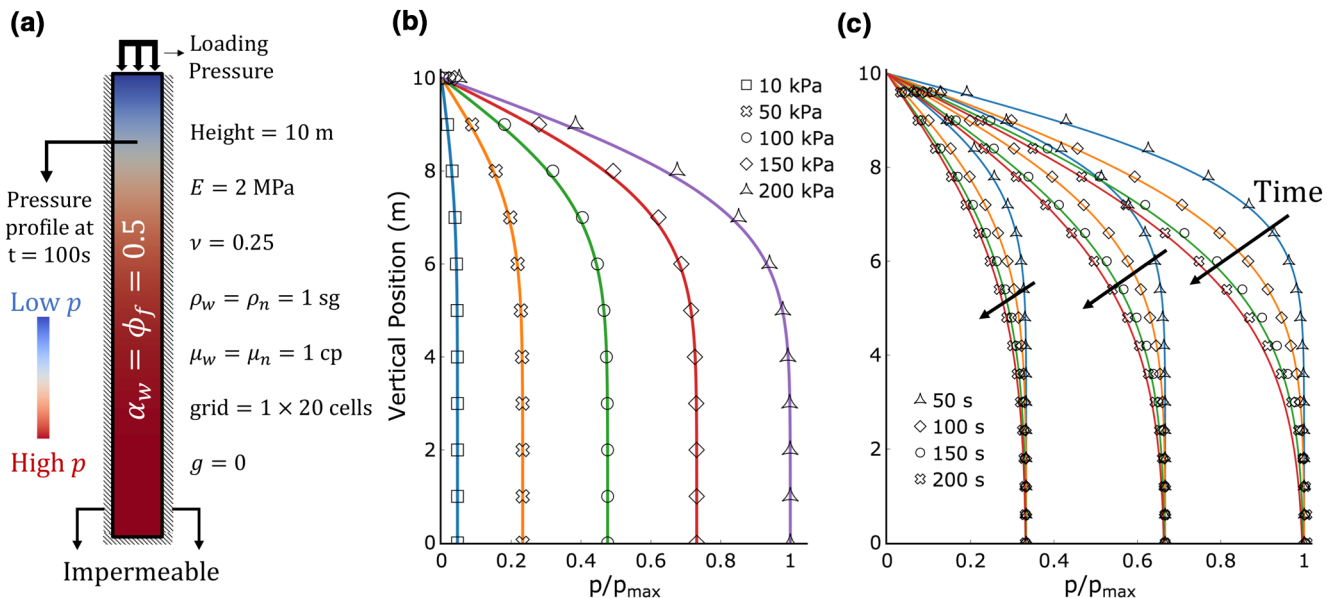


Figure 2. One-dimensional Terzaghi consolidation problem. (a) Simulation setup. (b) Analytical (solid lines) and numerical (symbols) pressure profiles at $t = 100$ s for different loading pressure values. (c) Time-dependent pressure profiles for different column porosity values (from left to right: $\phi_s = 0.25, 0.5, 0.75$).

confirms the applicability of the interfacial condition described in Section 2.4: as expected, solid stresses are dictated by standard elasticity theory in the porous region and become negligible in solid-free regions.

Given that the fluid-solid couplings in a poroelastic solid are now verified, we proceed to verify said terms for poro-visco-plastic materials.

4.3. Fluid Invasion and Fracturing in a Hele-Shaw Cell

The third verification case (and the first poro-visco-plastic case) consists in the qualitative replication of a set of fracturing experiments that examined the injection of aqueous glycerin into dry sand within a 30 by 30 by 2.5 cm Hele-Shaw cell (Huang et al., 2012a, 2012b). These experiments are inherently multiscale,

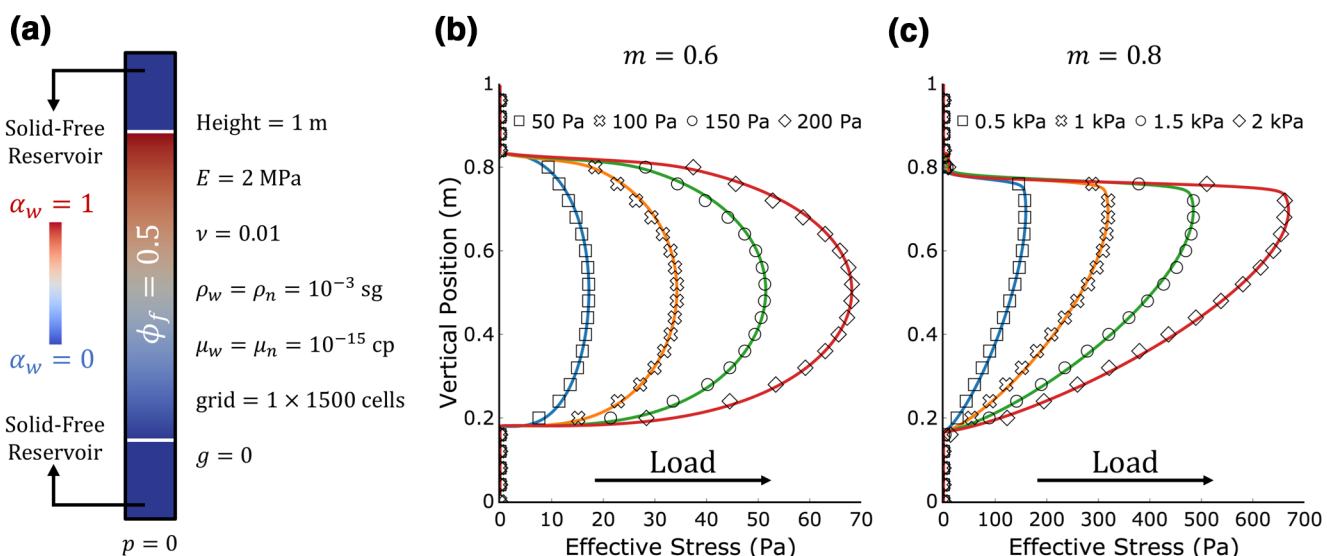


Figure 3. Capillary effects in a poroelastic column. (a) Simulation setup. (b and c) Analytical (solid lines) and numerical (symbols) effective stress profiles for different capillary pressure values ($p_{c,0} = 50\text{--}2,000$ Pa) and Van Genuchten coefficients ($m = 0.6$ and 0.8).

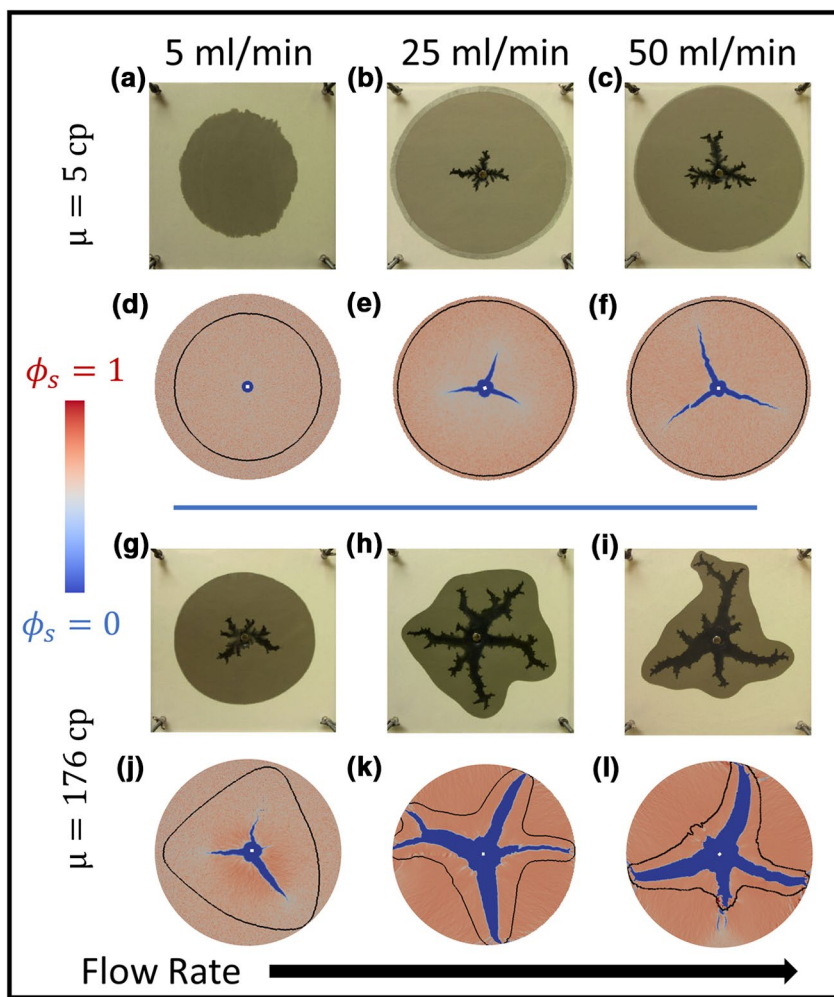


Figure 4. Comparison of experimental (a, b, c, g, h, i) and simulated (d, e, f, j, k, l) fracturing in a Hele-Shaw cell. The color bar represents the solid fraction within the simulations (where red implies a pure solid and blue pure fluids) and the black lines represent the advancing glycerin saturation front (defined as the contour where $\alpha_w = 0.99$). The experiments shown here are part of the results presented in Huang et al. (2012a).

in that the characteristic length scale of fractures in this system ($\sim\text{cm}$) is orders of magnitude larger than that of pores within the porous matrix ($\sim 100 \mu\text{m}$). They are also multiphysics, as they clearly exemplify the drag-controlled transition from Darcy flow within the porous medium to Stokes flow in the open fractures and the coupling between the hydrodynamics of fluid flow and the mechanics of fracture propagation (Figure 4).

The experimental setup involved the injection of aqueous glycerin at various flow rates, q , between 5 and 50 ml/min while also varying the fluid's viscosity, μ_{gly} , between 5 and 176 cp for different experiments. Our numerical simulations were parameterized using measured values of the glycerin-air surface tension ($\gamma = 0.063 \text{ kg/s}^2$), the density of pure glycerin ($\rho_{\text{gly}} = 1,250 \text{ kg/m}^3$), the density of air ($\rho_{\text{air}} = 1 \text{ kg/m}^3$), the viscosity of air ($\mu_{\text{air}} = 0.017 \text{ cp}$), and the average radius and density of sand grains ($100 \mu\text{m}$ and $2,650 \text{ kg/m}^3$, respectively). To mimic the sand's experimental configuration and permeability, the simulated solid fraction field was set to a random initial normal distribution such that $\phi_s = 0.64 \pm 0.05$ and the permeability was modeled as a function of the solid fraction through the Kozeny-Carman relation with $k_0 = 6.7 \times 10^{-12} \text{ m}^2$. Relative permeabilities were calculated through the Van Genutchen model with the Van Genuchten coefficient m set to 0.99 (see Appendix A), while capillary pressures were deemed negligible (as $2\gamma r^{-1} \ll \mu k^{-1} U_L$). Finally, the porous medium was modeled as a continuous Herschel-Bulkley-Quemada plastic (Appendix B).

with yield stress $\tau_0 = 16.02 \text{ m}^2/\text{s}^2$ (Quemada, 1977). Plasticity was used as the preferred mode of solid rheology due to its ability to account for the compressive and irreversible effects caused by fracturing within these experiments (Ahmed et al., 2007; van Dam et al., 2002).

Numerically speaking, the simulations were carried out in a 30 by 30 cm 2-D grid (500 by 500 cells) with constant velocity and zero-gradient pressure boundary conditions at the inlet, zero-gradient velocity and zero pressure boundary conditions at the boundary walls, and a solid velocity tangential slip condition at all boundaries (i.e., the solid cannot flow across the boundaries, but the fluids can). Each simulation was run in parallel for approximately 2.5 hours on a single 28-core node or until the injected glycerin reached the outer boundary. Lastly, to enable a closer comparison between our 2-D simulation and the 3-D experiment we added an additional drag term to the fluid momentum equation equal to $12\mu a^{-2}U_f$, which accounts for viscous dissipation through friction with the walls in a Hele-Shaw cell with aperture a (Ferrari et al., 2015).

As shown in Figure 4, a dramatic transition in the mode of fluid invasion is observed with increasing fluid injection velocity and viscosity. At low flow rates and low viscosity ($q = 5 \text{ ml/min}$, $\mu = 5 \text{ cp}$), there is no discernible solid deformation and the main mode of fluid flow is through uniform invasion of the porous medium (Figure 4a). At intermediate flow rates and low viscosity ($q = 25 \text{ ml/min}$ to 30 ml/min , $\mu = 5 \text{ cp}$), we still observe a uniform invasion front, but small fractures begin to appear (Figures 4b and 4c). At high viscosity ($\mu = 176 \text{ cp}$), we see clear fracturing patterns preceded by a nonuniform fluid invasion front (Figures 4h and 4i).

Figure 4 shows that our simulation predictions are qualitatively consistent with the experiments presented in Huang et al. (2012a) with regard to both the stability of the capillary displacement front and the observed fracturing transition behavior. As suggested above, accurate prediction of this transition requires not only proper handling of fluid-fluid interactions (surface tension and relative permeability effects), but also accurate descriptions of their relationship with solid mechanics (drag) and the proper implementation of a solid rheological model that can replicate irreversible and unstable fracturing processes. We note that in our simulations, fracture initialization and propagation are predicted based on continuum-scale equations for the rheology and mechanics of the bulk porous solid, with no specific treatment of grain-scale mechanics. Grid-level instabilities are brought about by the normally distributed porosity and permeability fields, as shown in Appendix C. The microstructural differences between the experiments and our simulations (most clear in Figures 4c, 4f, 4h, and 4k) likely arise at least in part from the fact that the solid is modeled as a continuum rather than a granular material.

This section demonstrates that the multiphase DBB model can be used to replicate and predict the main mode of fluid flow and solid deformation within fracturing systems. A comprehensive study of the controlling parameters for multiphase fracturing in the presence of both viscous and capillary stresses will be the focus of an adjacent study.

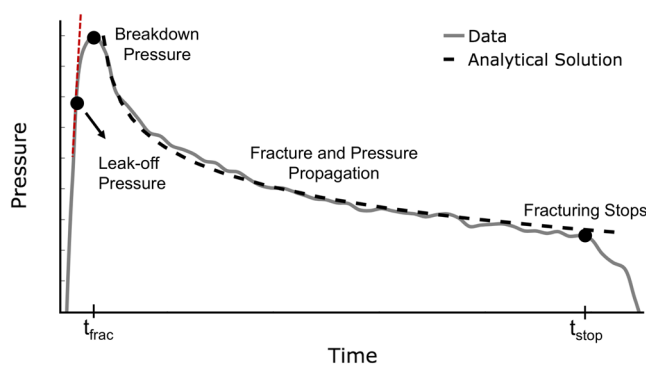


Figure 5. Conceptual representation of wellbore pressure evolution during fluid-induced fracturing of low-permeability rocks. In this section, we are interested in modeling the behavior between t_{frac} and t_{stop} .

4.4. Modeling Fracturing Wellbore Pressure

Having shown that our model can qualitatively predict fracturing behavior, we now aim to determine whether it can do so in a quantitative manner. As depicted in Figure 5, fluid-induced fracturing of low-permeability rocks proceeds through the following well-established series of events: First, fluid pressure increases linearly as fracturing fluid is injected into the wellbore. Second, as wellbore pressure increases and approaches the leak-off pressure, a small amount of pressure is propagated by fluid leakage into the rock. Third, fluid pressure continues to increase until it reaches the breakdown pressure, at which point it is high enough to fracture the rock. Fourth, a fracture is initiated and propagates; the wellbore pressure slowly decreases. Fifth, injection stops, fracture propagation stops, and wellbore pressure rapidly dissipates (Abass et al., 2007; Ahmed et al., 2007; Huang et al., 2012a; Papanastasiou, 2000; Santillán et al., 2017).

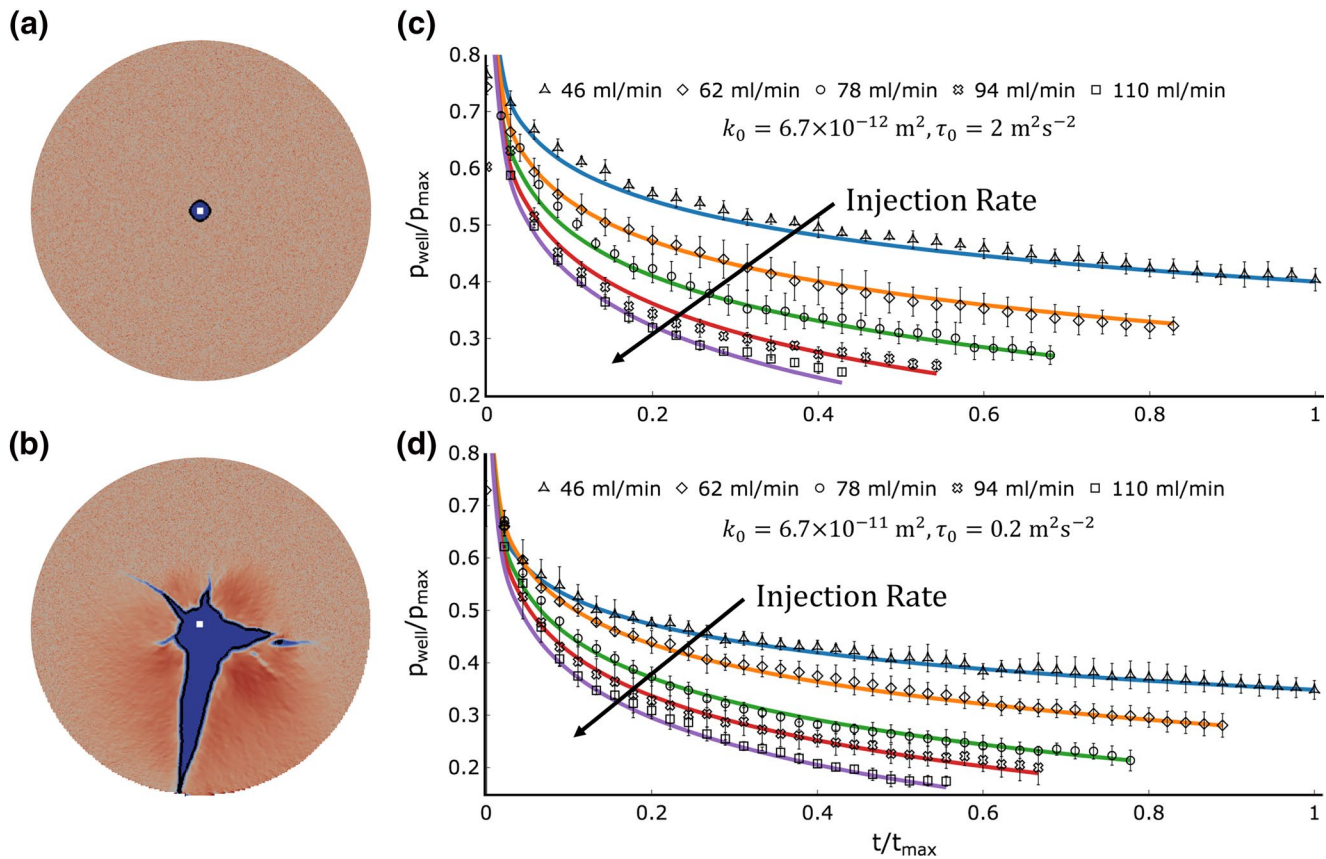


Figure 6. Wellbore pressure as a function of injection rate and time. (a) The initial simulation setup showing the initial wellbore radius $r_{\text{well}} = 1.3 \text{ cm}$, as well as the normally distributed solid fraction field. (b) The fractured system, where the thin black line represents the position of the advancing glycerin saturation front. (c and d) show the wellbore pressure as a function of time for different flow rates and different combinations of solid yield stress and permeability. Solid curves represent analytical solutions, while symbols represent simulation predictions. The color scheme in (a and b) is the same as in Figure 4, and p_{max} is the maximum analytically predicted pressure in each simulation.

In this section, we aim to numerically replicate the time-dependent fracturing wellbore pressure during fracture propagation (i.e., the fourth stage outlined above) as described by an analytical solution presented in Barros-Galvis et al. (2017).

$$p_{\text{well}} = p_0 - \frac{\mu q}{4\pi k_0 h} \left[\ln \left(\frac{tk_0\tau_0}{\phi_f \mu r_{\text{well}}^2} \right) + 0.81 \right] \quad (41)$$

where t is the time elapsed since fracture initialization, q is the fluid injection rate, p_{well} is the wellbore pressure, p_0 is the minimum pressure required for starting a fracture (a function of the solid's yield stress τ_0), h is the formation thickness, and r_{well} is the wellbore radius. The remaining variables follow the same definitions described earlier. The general numerical setup is almost identical to the one presented in the previous section. The key difference is that we now inject aqueous glycerin into a strongly non wetting (and thus almost impermeable) porous material. This is done to ensure an accurate replication of the analytical solution and its related assumptions, where fracturing is the main mode of fluid flow and there is virtually no fluid invasion into the porous matrix. The exact simulation parameters are $q = 46\text{--}110 \text{ ml/min}$, $\tau_0 = 0.2 \text{ or } 2 \text{ m}^2/\text{s}^2$, $k_0 = 6.7 \times 10^{-11} \text{ or } 6.7 \times 10^{-12} \text{ m}^2$, $\mu_{\text{gly}} = 5 \text{ cp}$, and $m = 0.05$. Note that low values of m indicate that the porous formation is strongly nonwetting to the injected fluid (see Figure S4 in the SI for the resulting relative permeability curve). All other parameters are as in the previous section.

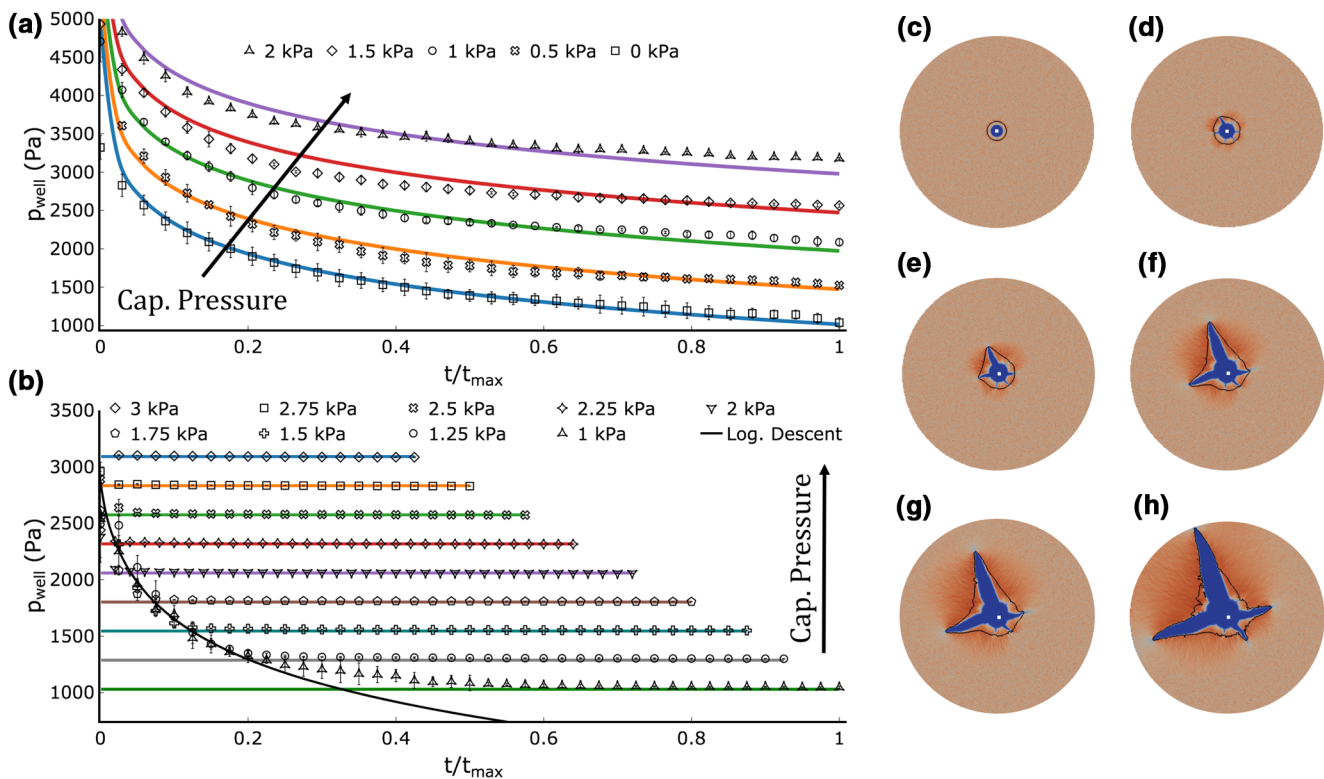


Figure 7. Effect of capillary entry pressure on fracturing wellbore pressure. (a and b) Wellbore pressure as a function of time and entry pressure for low and high permeability systems, respectively. In (b), curves at increasingly high pressures were cut off for illustrative purposes and the solid line represents a fitted reference logarithmic pressure descent curve. (c–h) Time evolution of fractured system with a 1 kPa capillary entry pressure and high permeability. (c) Initial fluid invasion ($t/t_{\max} < 0$): At early times, the wellbore pressure rises rapidly and becomes larger than the entry capillary pressure. The fluid invades the porous formation symmetrically. (d) Fracture initiation ($t/t_{\max} = 0$): The wellbore pressure continues to rise until it is larger than the breakdown pressure, at which point small fractures start to form. Fluid invasion continues. (e and f) Fracture propagation ($t/t_{\max} > 0 | P_{\text{well}} > p_{c,0}$): The wellbore pressure drops as fractures propagate. Fluid invasion continues asymmetrically around said fractures. (g) Fluid invasion stops ($t/t_{\max} > 0 | P_{\text{well}} \sim p_{c,0}$): As the wellbore pressure keeps dropping, the entry capillary pressure condition at the porous interface ensures that that wellbore pressure never goes below $p_{c,0}$, at which point fluid invasion stops. (h) Fracture reaches the simulation boundary ($t/t_{\max} = 1$). The color convention in Figures (c–h) is the same as in Figure 4.

Lastly, as hinted at before, a notable characteristic of our model is that different normally-distributed solid fraction field initializations give different fracturing results (Appendix C). For this reason, we performed four simulations for each parameter set. In Figure 6, we present the average predicted wellbore pressure evolution with errors bar representing the 95% confidence interval.

Figure 6 shows that our model can accurately and reliably predict the pressure and deformation behavior of a variety of fracturing systems, as all curves exhibit excellent agreement with their respective analytical solution. Note that the length of each curve relates inversely to the injection speed. This is because fractures at higher injection rates consistently reach the system's boundary faster than their counterparts, at which point there is a sharp decrease in pressure and the analytical solution no longer applies. Therefore, each curve's cutoff point represents the time at which the fracture effectively becomes an open channel between the wellbore and the outer boundary, normalized to the average value of that time for the slowest-moving fracture (i.e., $t = t_{\max}$).

The successful replication of the analytical pressure profiles in this section verifies the model components pertaining to the pressure-velocity-deformation coupling and the two-way momentum transfer between the fluid and solid phases (drag). Therefore, the only model component left to verify is the implementation of the capillary force terms during fracturing of a plastic solid.

4.5. Capillary Effects on Fracturing Wellbore Pressure

Our fifth verification systematically varies the capillary entry pressure within nonwetting fracturing systems to quantify its effects on wellbore pressure. For this, we consider two different complementary cases: one where capillary forces are comparable to their viscous counterparts, and another where they are significantly larger than them. All parameters are the same as in the previous experiments (Section 4.4) unless otherwise specified.

The first set of experiments expands the previous analysis (Section 4.4) into strongly nonwetting systems with the addition of a constant capillary pressure jump at the fracture interface imposed by a flat capillary pressure curve ($p_c = p_{c,0} = 0\text{--}2 \text{ kPa}$, $\tau_0 = 2 \text{ m}^2/\text{s}^2$, $k_0 = 6.7 \times 10^{-12} \text{ m}^2$, $m = 0.05$, and $q = 78 \text{ ml/min}$). In this case, all the assumptions present in the fracturing analytical solution (Equation 41) are satisfied. However, said solution still does not account for capillarity. For constant flow in nonwetting systems, the addition of a constant capillary entry pressure jump at the fluid-solid interface would increase the calculated propagation pressure in Equation 41 by said value such that $p_{\text{well}}^{\text{new}} = p_{\text{well}} + p_c$. This effect is exemplified in Figure 7a, where we present the updated analytical results in conjunction with our equivalent numerical results, demonstrating excellent agreement between them. Note that the predicted linear relationship between wellbore pressure and capillary entry pressure is not explicitly imposed in the numerical model. On the contrary, it arises naturally from the balance of viscous, capillary, and structural forces in Equations 25–29.

The second set of experiments modifies the previous experiments by making the porous medium significantly more permeable, while still maintaining a constant capillary pressure jump at the fracture interface ($p_c = p_{c,0} = 1\text{--}3 \text{ kPa}$, $\tau_0 = 0.2 \text{ m}^2/\text{s}^2$, $k_0 = 6.7 \times 10^{-11} \text{ m}^2$, $m = 0.99$, and $q = 78 \text{ ml/min}$). This results in a set of cases where the wellbore pressure is increasingly controlled by the capillary pressure drop rather than by the viscous pressure drop across the fracture and porous formation.

Figure 7 demonstrates precisely this effect. Our simulations show that the wellbore pressure always decays toward the capillary entry pressure once viscous effects are dissipated by fracture growth, that is, we observe a transition between viscous- and capillary-dominated regimes. At low values of $p_{c,0}$ ($<2500 \text{ Pa}$) the entry pressure is not high enough to prevent fluid flow into the surrounding porous matrix during fracturing (Figures 7b–7h). The resulting pressure drop cannot be modeled by the previously presented analytical solution (as it violates the no leak-off assumption), but still follows a logarithm-type curve that is characteristic of flow in fracturing systems. With increasing fracture propagation, the viscous pressure drop decreases until the wellbore pressure equals the entry pressure, which is, by definition, the minimum pressure drop required for fluid flow in highly permeable nonwetting systems. Finally, we note that in cases where capillary entry pressure is high relative to the pressure required to fracture the solid (i.e., at $(p_{c,0} > 2.250 \text{ Pa}$ in the conditions simulated in Figure 7b), fracturing begins before the wellbore pressure can exceed $p_{c,0}$. This prevents essentially all flow into the porous formation, and the wellbore pressure is immediately stabilized at $\sim p_{c,0}$. For all cases, fractures continue to propagate until they reach the system boundary, at which point the pressure drops rapidly as noted in Section 4.4.

In this section, we reduced the inherent complexity of the model's capillary force terms $F_{c,i}$ (Equations 31 and 32) into a simple set of intuitive verifications. The quantitative agreement between these two analytical cases and their corresponding numerical simulations validate the implementation of the impact of capillary pressure effects on the mechanics of a ductile porous solid within our model.

5. Illustrative Applications

Having verified and tested the model, we now proceed with two illustrations that demonstrate how *hybrid-BiotInterFoam* enables the simulation of relatively complex coupled multiphase multiscale systems. The following cases serve as illustrative examples of our model's features and capabilities as well as tutorial cases within the accompanying toolbox.

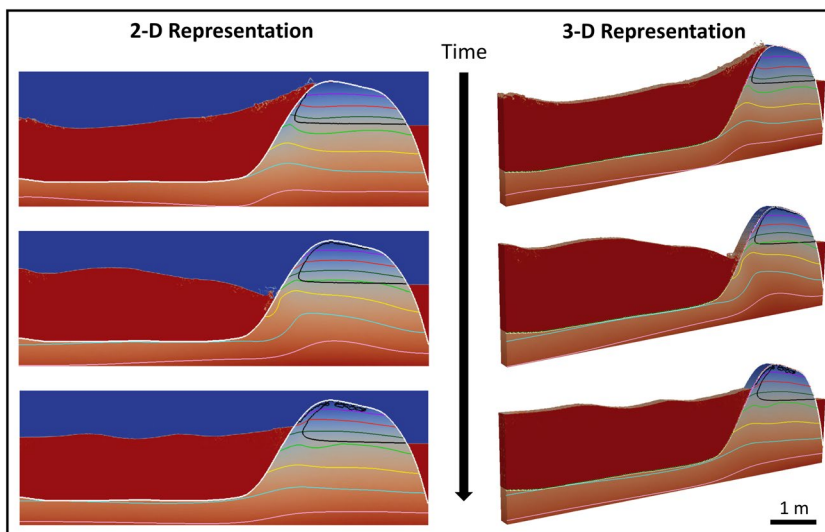


Figure 8. Waves crashing against a poroelastic coastal barrier. Here, the thin black line represents the water-air interface ($\alpha_w = 0.5$) within the barrier and red-blue colors represent water and air outside the barrier. Colored contours within the barrier are the calculated Von Mises stresses and are shown in 5 kPa increments in the general downwards direction. Note that the largest stresses are seen during the initial wave crash and increase toward the base of the barrier due to gravitational effects.

5.1. Elastic Failure in Coastal Barriers

Coastal barriers are ubiquitous features in coastal infrastructure development. When designed appropriately, these structures can be very effective in regulating water levels and protecting against inclement weather (Morton, 2002). However, accurate prediction of the coupled fluid-solid mechanics of these structures (which can lead to barrier failure) is inherently challenging as it requires modeling large-scale features (waves) while also considering small-scale viscous and capillary interactions within the barrier.

The following case represents the continuation of the three-dimensional coastal barrier illustration presented in Carrillo et al. (2020) with the addition of linear-elastic poromechanics. As such, the simulation was created by initializing a heterogeneous porosity field (with $k_0 = 2 \times 10^{-8} \text{ m}^2$ and $\phi_f = 0.5$) in the shape of a barrier within a 8.3 by 2.7 by 0.25 m rectangular grid with over 43 million cells (1600 by 540 by 50 cells). The relevant solid mechanics parameters were $E = 5 \text{ MPa}$, $\nu = 0.45$, and $\rho_s = 2350 \text{ kg/m}^3$. Relative permeabilities and capillary pressures were evaluated through the Van Genuchten model with $m = 0.8$ and $p_{c,0} = 1 \text{ kPa}$. Before the start of the simulation, the water level was set to partially cover the barrier and then allowed to equilibrate. A single wave was then initialized at $t = 0$. This results in a simulation that exhibits a clear wave absorption cycle that gradually dissipates in time, as seen in Figure 8. Detailed discussion on the fluid mechanics of this problem can be found in Carrillo et al. (2020). In total, this 3-D simulation lasted for 15 simulated seconds, which took approximately 30 hours to run on 16 computational nodes with 28-Broadwell Xeon cores each.

Here, however, we are interested in evaluating the barrier's propensity to failure. We do this by applying the Von Mises yield criterion, which is commonly used to predict material failure in elastic systems. It states that if the second invariant of the solid's deviatoric stress (the Von Mises stress) is greater than a critical value (the yield strength) the material will begin to deform nonelastically (Von Mises, 1913). Although we do not specify said critical value within our simulations, we can map the time-evolution of Von Mises stresses within the coastal barrier as a result of a wave absorption cycle (Figure 8). Our results illustrate the potential utility of our simulation framework in predicting the location and time-of-formation of stress induced defects within coastal barrier as a function of wave characteristics, permeability, and barrier geometry.

5.2. Flow-Induced Surface Deformation

Surface deformation due to subsurface fluid flow is a common geological phenomenon occurring in strongly coupled systems and has clear implications in studies related to induced seismicity (Shapiro & Dinske, 2009), CO₂ injection in the subsurface (Morris et al., 2011), land subsidence (Booker & Carter, 1986), and the formation of dikes and volcanoes (Abdelmalak et al., 2012; Mathieu et al., 2008). In order to properly model these systems, it is necessary to be able to capture the time-evolution of surface uplift, cracks, and hydraulic fractures, as well as the effects that these features have on the overall flow field. Here, we use the terms hydraulic fracture versus crack to refer to solid failure at versus away from the injected fluid, respectively.

This illustrative case was inspired by the experiments reported by Abdelmalak et al. (2012), where the authors injected a highly viscous fluid into a dry silica powder in a Hele-Shaw cell in order to study the impact of hydraulic fractures on surface deformation, for example, during the creation of volcanic structures. The system also bears some analogy to situations involving the injection of fluids into subsurface reservoirs, for example, during geologic CO₂ sequestration (Rutqvist, 2012). The base case of our simulations consists of an impermeable rectangular container (50 by 30 cm, 500 by 300 cells) that is open to the atmosphere, is partially filled with a dry porous medium ($\phi_s = 0.6 \pm 0.05$, $\rho_s = 2650 \text{ kg/m}^3$, $k_0 = 5 \times 10^{-11} \text{ m}^2$), and has an injection well at its lower boundary that injects water at $q = 6.5 \text{ ml/s}$ (Figure 9). To account for irreversible solid deformation, the porous medium is modeled as a plastic with yield stress $\tau_0 = 0.22 \text{ m}^2/\text{s}^2$. The solid is represented as impermeable to the invading fluid through the use of the Van Genuchten model with $m = 0.05$ and $p_c = 0$. Then, using this base case as a standard, we individually varied each of the main parameters (q , k_0 , τ_0 , m , ϕ_s , μ_{water}) over several simulations in order to model the resulting solid deformation processes: fracturing, cracking, surface uplift, and subsidence (Figure 9).

The resulting cases demonstrate that cracking (solid failure away from the injected fluid) is strictly dependent on the number and orientation of existing hydraulic fractures, as it only occurs when there is more than one fracture branching off from the main injection point (Figures 9b–9d, 9h, and 9l). This is likely because in cases presenting a single vertical fracture solid displacement is almost exclusively perpendicular to the fracturing direction, leading to virtually no surface deformation or cracking (Figures 9a, 9e, and 9m). Contrastingly, the creation of inclined fractures exerts vertical forces on the solid, resulting in surface uplift and crack formation. The above diagram strongly suggests that deformation is controlled by the balance between viscous and structural forces: larger fractures occur within softer solids with higher momentum transfer, and smaller fractures occur in tougher solids with lower momentum transfer. As stated above, a comprehensive examination of the parameters that control solid fracturing will be the focus of an adjacent paper.

In addition to the surface uplift presented above, subsurface subsidence is observed in the simulated system in conditions where the porous solid is rendered permeable to the invading fluid (i.e., $m \gg 0.05$). This phenomenon is not primarily controlled by momentum transfer, but rather by a gravitational effect whereby the displacement of air by water within the porous medium around the advancing hydraulic fracture renders the solid-fluid mixture heavier. Once it is heavy enough to overcome the plastic yield stress, the solid subsides and compresses around the fluid source (Figure 9m).

With these last two illustrative examples, we have shown that our modeling framework is flexible and readily applicable to a large variety of cases within elastic and plastic systems. We invite the interested reader to tune, adapt, and expand the present illustrative simulations, which are included in the accompanying CFD toolbox.

6. Conclusions

We derived, implemented, benchmarked, and applied a novel CFD package for simulation of multiphase flow within and around deformable porous media. This microcontinuum modeling framework is based on elementary physics and was rigorously derived through the method of volume averaging and asymptotic matching to the multiphase Volume-of-Fluid equations in solid-free regions and multiphase Biot Theory in porous regions. The result is a single set of partial differential equations that is valid in every

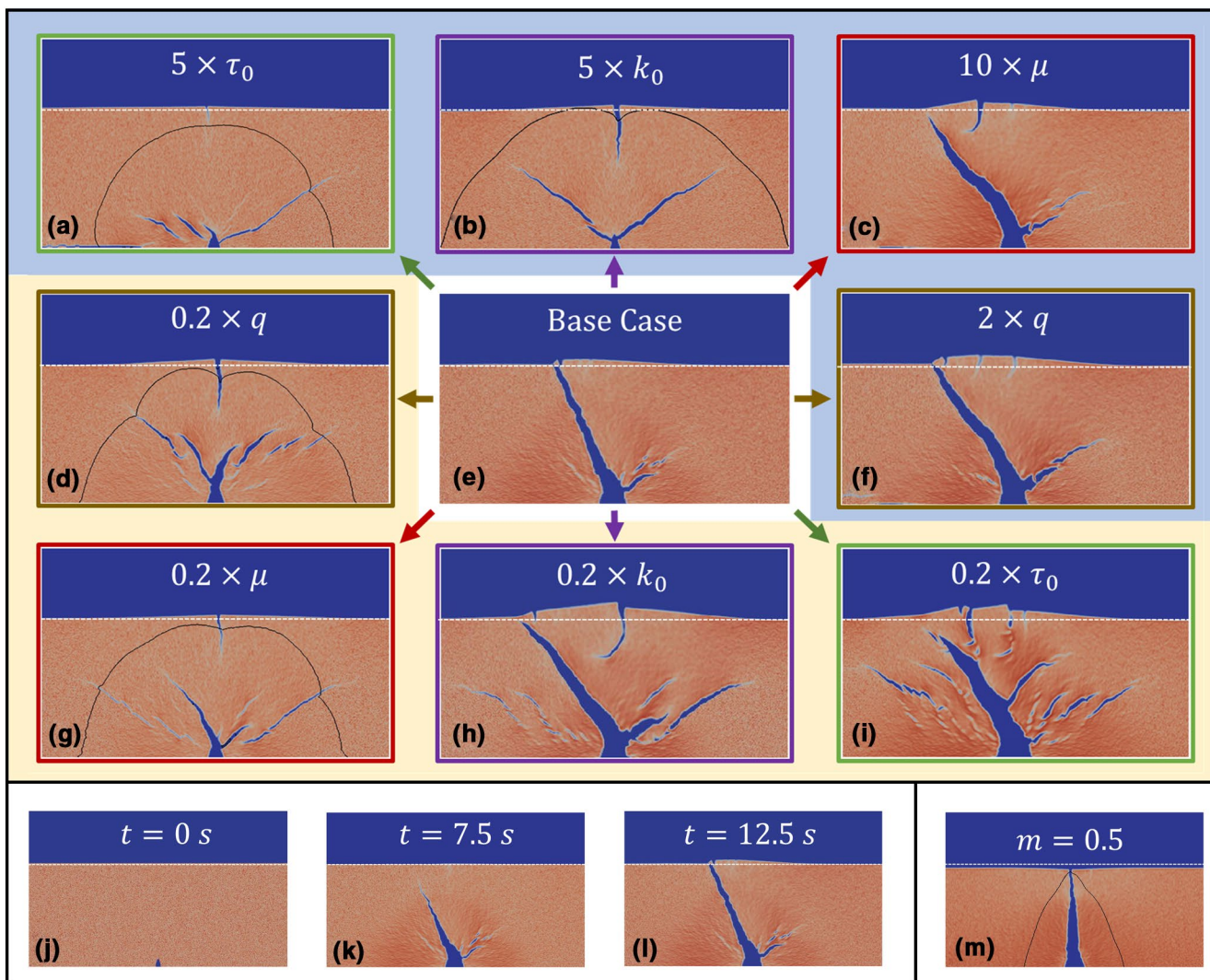


Figure 9. Study of the impact of subsurface fluid injection on hydraulic fracturing, cracking, and surface deformation. (a–i) Representative cases showing the effects of changing permeability k_0 (purple), solid yield stress τ_0 (green), injection rate q (brown), and injected fluid viscosity μ (red) on surface deformation. The blue and yellow subsections contain the results of increasing or decreasing the controlling parameters, respectively. (j–l) Time evolution of the fracturing base case. (m) Surface subsidence example. The difference between the base case (e) and all other simulations is shown in each case's legend. Dotted white lines represent the surface height of the initial solid fraction configuration. Note that the color scheme in all simulations is the same as in Figure 4.

simulated grid cell, regardless of content, which obviates the need to define different meshes, domains, or complex interfacial conditions within the simulation. The solver's numeric and algorithmic development were discussed and implemented into *hybridBiotInterFoam*, an open-source package accessible to any interested party.

Throughout this study and its predecessors (Carrillo & Bourg, 2019; Carrillo et al., 2020), we show that the Multiphase DBB model can be readily used to model a large variety of systems, from single-phase flow in static porous media, to elastic systems under compression, to viscosity- or capillarity-dominated fracturing systems, to multiscale wave propagation in poroelastic coastal barriers.

We note, however, that the solver presented here cannot be liberally applied to any porous system, as it comes with the following inherent limitations. First, closure of the system of equations requires appropriate constitutive and parametric relations that describe fluid pressure, permeability, capillarity, and rheo-

ogy within volume-averaged porous regions. Therefore, the assumptions present in each of these models should be carefully considered. Second, volume averaging imposes important length scale restrictions in order to fulfill the scale-separation hypothesis, where the pore sizes within the averaging volume must be substantially smaller than the chosen REV, and the REV must be substantially smaller than the macroscopic length scale. Third, as currently implemented, the multiphase DBB framework only represents continuum-level elastic or plastic solid mechanics that can be described from an Eulerian frame of reference. As such, it cannot be used to model large elastic deformations or phenomena originating from sub-REV heterogeneities such as fluidization or granular mechanics (Meng et al., 2020), except insofar as they are captured in an averaged manner at the REV scale. Fourth, the use of the CSF as a representation of capillary forces within solid-free regions enforces mass conservation, but it creates a diffuse fluid-fluid interface that may generate spurious and parasitic currents.

Finally, although the modeling framework developed here opens up significant new possibilities in the simulation of coupled fluid-solid mechanics, it also creates a need for the development of constitutive relations describing the coupling between multiphase flow and poromechanics. Of particular importance is the formulation of saturation and deformation-dependent solid rheological models (both plastic and elastic), as well as the rigorous derivation of the interfacial condition between solid-free and deformable porous regions. In this study, we proposed a suitable approximation for said condition based on our single-field formulation, the implementation of a wettability interfacial condition, and the previous work done by Neale and Nader (1974) and Zampogna et al. (2019). However, the accuracy and validity of such an approximation is still an open question, one that is at the frontier of our modeling and characterization capabilities (Qin et al., 2020). The derivation and implementation of said interfacial condition, along with the addition of erosion and chemical reactions into this modeling framework, will be the focus of subsequent papers.

Appendix A: Relative Permeability and Capillary Pressure Models

A1 Relative Permeability Models

The two relative permeability models used in this paper and implemented in the accompanying code depend on defining an effective saturation in order to account for the presence of irreducible saturations within a porous medium

$$\alpha_{w,eff} = \frac{\alpha_w - \alpha_{w,irr}}{1 - \alpha_{w,irr} - \alpha_{w,irr}}$$

here, $\alpha_{w,eff}$ is the wetting fluid's effective saturation, which is the wetting fluid's saturation normalized by each fluid's irreducible saturation $\alpha_{i,irr}$. The Brooks and Corey (1964) model relates each phase's relative permeability to saturation through the following expressions

$$k_{r,n} = (1 - \alpha_{w,eff})^m$$

$$k_{r,w} = (\alpha_{w,eff})^m$$

where m is a nondimensional coefficient that controls how sensitive the relative permeability is with respect to saturation. The van Genuchten (1980) model calculates relative permeabilities in the following way

$$k_{r,n} = (1 - \alpha_{w,eff})^{\frac{1}{2}} \left((1 - \alpha_{w,eff})^{\frac{1}{m}} \right)^{2m}$$

$$k_{r,w} = (\alpha_{w,eff})^{\frac{1}{2}} \left(1 - \left(1 - (\alpha_{w,eff})^{\frac{1}{m}} \right)^m \right)^2$$

In this case, m controls how wetting (or nonwetting) the porous medium is to a given wetting (or nonwetting) fluid. High values of m indicate high relative permeabilities for the nonwetting fluid, while low values of m indicate very low relative permeabilities for the same fluid.

A2 Capillary Pressure Models

The implemented capillary pressure models also depend on an effective wetting-fluid saturation $\alpha_{w,pc}$,

$$\alpha_{w,pc} = \frac{\alpha_w - \alpha_{pc,irr}}{\alpha_{pc,max} - \alpha_{pc,irr}}$$

here, $\alpha_{pc,max}$ is the maximum saturation of the wetting fluid and $\alpha_{pc,irr}$ is its irreducible saturation. The Brooks and Corey (1964) model uses the following expression to calculate the capillary pressures within a porous medium

$$p_c = p_{c,0} (\alpha_{w,pc})^{-\beta}$$

where $p_{c,0}$ is the entry capillary pressure, and β is a parameter depending on the pore size distribution. Conversely, the van Genuchten (1980) model calculates the capillary pressure with the following relation

$$p_c = p_{c,0} \left((\alpha_{w,pc})^{-\frac{1}{m}} - 1 \right)^{1-m}$$

Appendix B: Solid Rheology Models

B1 Hershel-Bulkley Plasticity

A Bingham plastic is a material that deforms only once it is under a sufficiently high stress. After this yield stress is reached, it will deform viscously and irreversibly. The Herschel-Bulkley rheological model combines the properties of a Bingham plastic with a power-law viscosity model, such that said plastic can be shear thinning or shear thickening during deformation. In OpenFOAM®, this model is implemented as follows:

$$\boldsymbol{\sigma} = \mu_s^{eff} \left(\nabla \mathbf{U}_s + (\nabla \mathbf{U}_s)^T - \frac{2}{3} \nabla \cdot (\mathbf{U}_s \mathbf{I}) \right)$$

where μ_s^{eff} is the effective solid plastic viscosity, which is then modeled through a power-law expression:

$$\mu_s^{eff} = \min \left(\mu_s^0, \frac{\tau}{\eta} + \mu_s \eta^{n-1} \right)$$

where μ_s^0 is the limiting viscosity (set to a large value), τ is the yield stress, μ_s is the viscosity of the solid once the yield stress is overcome, n is the flow index ($n = 1$ for constant viscosity), and η is the shear rate.

B2 Quemada Rheology Model

The Quemada rheology model (Quemada, 1977; Spearman, 2017) is a simple model that accounts for the fact that the average yield stress and effective viscosity of a plastic are functions of the solid fraction. These

two quantities are large at high solid fractions and small at low solid fractions, as described by the following relations

$$\tau = \tau_0 \left(\frac{\left(\phi_s / \phi_s^{max} \right)}{\left(1 - \phi_s / \phi_s^{max} \right)} \right)^D$$

$$\mu_s = \frac{\mu_0}{\left(1 - \frac{\phi_s}{\phi_s^{max}} \right)^2}$$

here, ϕ_s^{max} is the maximum solid fraction possible (perfect incompressible packing), τ_0 is the yield stress at $\phi_s = \phi_s^{max} / 2$, μ_0 is the viscosity of the fluid where the solid would be suspended at low solid fractions (high fluid fractions), and D is a scaling parameter based on the solid's fractal dimension.

B3 Linear Elasticity

A linear elastic solid model assumes that a solid exhibits very small reversible deformations under stress. Linear elasticity is described by the following relation:

$$\sigma = \mu_s \nabla u_s + \mu_s (\nabla u_s)^T + \lambda_s \text{tr}(\nabla u_s) I$$

where u_s is the solid displacement vector (not to be confused with solid velocity $U_s = \frac{\partial u_s}{\partial t}$), and μ_s and λ_s are the Lamé coefficients. The implementation of linear elasticity in OpenFOAM® follows the procedure outlined in Jasak and Weller (2000).

Appendix C: Fracturing Instabilities

The following figures demonstrate how different fracturing patterns can result from different solid fraction initializations. Here we carried out two sets of four identical experiments. In the first set, the only difference between cases is the value of the standard deviation of their respective normally distributed solid fraction field (all centered at $\phi_s = 0.64$). These experiments follow the same simulation setup used for the fracturing case shown in Figure 4k.

In the second set of experiments we simulated the base case presented in Figure 9 with different solid fraction profiles picked from the same normal distribution $\phi_s = 0.6 \pm 0.05$.

Figures A and B clearly show that the created fractures are dependent on the initial solid fraction distribution.

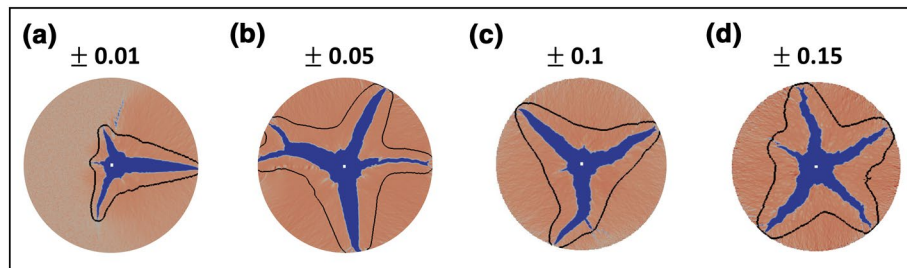


Figure A. Effects of the solid fraction field's standard deviation on fracturing. (a-d) Final porosity profiles for simulations with different initial solid fraction profiles, where the numbers on top of each sample indicated the initial standard deviation of each profile.

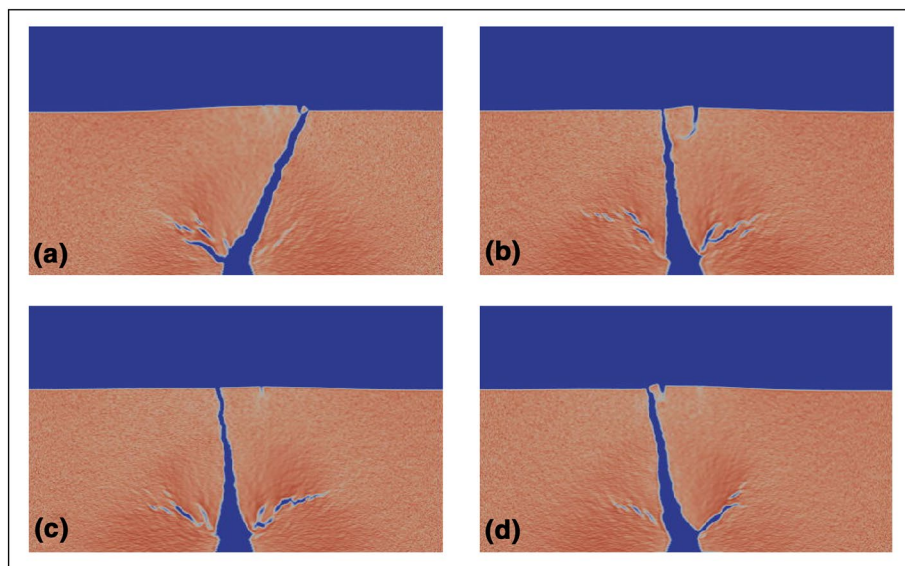


Figure B. Effects of different solid fraction field initializations on fracturing.

Data Availability Statement

A full compilation of the data and code used in this manuscript is archived at <https://doi.org/10.5281/zenodo.4013969> (Carrillo & Bourg, 2020) and can also be found at <https://github.com/Franjcf>.

Acknowledgments

This work was predominantly supported by the National Science Foundation, Division of Earth Sciences, Early Career program through Award EAR-1752982. FJC acknowledges additional support from the High Meadows Environmental Institute at Princeton University through the Mary and Randall Hack '69 Research Fund. We do not report any conflicts of interest.

References

- Abass, H., Hedayati, S., & Meadows, D. (2007). Nonplanar fracture propagation from a horizontal wellbore: Experimental study. *SPE Production & Facilities*, 11(03), 133–137. <https://doi.org/10.2118/24823-pa>
- Abdelmalak, M. M., Mourques, R., Galland, O., & Bureau, D. (2012). Fracture mode analysis and related surface deformation during dyke intrusion: Results from 2D experimental modelling. *Earth and Planetary Science Letters*, 359–360, 93–105. <https://doi.org/10.1016/j.epsl.2012.10.008>
- Abou-Sayed, A., Zaki, K., Wang, G., Meng, F., & Sarfare, M. (2007). *Fracture propagation and formation disturbance during injection and frac-pack operations in soft compacting rocks* (pp. 3453–3464). Proceedings—SPE Annual Technical Conference and Exhibition, Society of Petroleum Engineers, Houston, TX. <https://doi.org/10.2523/90656-ms>
- Auton, L. C., & MacMinn, C. W. (2017). From arteries to boreholes: Steady-state response of a poroelastic cylinder to fluid injection. *Proceedings of the Royal Society A: Mathematical, Physical & Engineering Sciences*, 473(2201), 20160753. <https://doi.org/10.1098/rspa.2016.0753>
- Baber, K., Flemisch, B., & Helmig, R. (2016). Modeling drop dynamics at the interface between free and porous-medium flow using the mortar method. *International Journal of Heat and Mass Transfer*, 99, 660–671. <https://doi.org/10.1016/j.ijheatmasstransfer.2016.04.014>
- Bächer, C., & Gekle, S. (2019). Computational modeling of active deformable membranes embedded in three-dimensional flows. *Physical Review E*, 99(6), 062418. <https://doi.org/10.1103/PhysRevE.99.062418>
- Barros-Galvis, N., Fernando Samaniego, V., & Cinco-Ley, H. (2017). Fluid dynamics in naturally fractured tectonic reservoirs. *Journal of Petroleum Exploration and Production Technology*, 8(1), 1–16. <https://doi.org/10.1007/s13202-017-0320-8>
- Barry, S. I., Mercer, G. N., & Zoppou, C. (1997). Deformation and fluid flow due to a source in a poro-elastic layer. *Applied Mathematical Modelling*, 21(11), 681–689. [https://doi.org/10.1016/S0307-904X\(97\)00097-8](https://doi.org/10.1016/S0307-904X(97)00097-8)
- Beavers, G. S., & Joseph, D. D. (1967). Boundary conditions at a naturally permeable wall. *Journal of Fluid Mechanics*, 30(1), 197–207. <https://doi.org/10.1017/S0022112067001375>
- Biot, M. A. (1941). General theory of three-dimensional consolidation. *Journal of Applied Physics*, 12(2), 155–164. <https://doi.org/10.1063/1.1712886>
- Bock, H., Dehandschutter, B., Martin, C. D., Mazurek, M., De Haller, A., Skoczyłas, F., & Davy, C. (2010). *Self-sealing of fractures in argillaceous formations in the context of geological disposal of radioactive waste: Review and synthesis* (Tech. Rep. No. NEA No. 6184). Paris, France: Nuclear Energy Agency.
- Booker, J. R., & Carter, J. P. (1986). Long term subsidence due to fluid extraction from a saturated, anisotropic, elastic soil mass. *Quarterly Journal of Mechanics & Applied Mathematics*, 39(1), 85–98. <https://doi.org/10.1093/qjmam/39.1.85>
- Bottero, S., Picoreanu, C., Enzien, M., Van Loosdrecht, M. C., Bruining, H., & Heimovaara, T. (2010). Formation damage and impact on gas flow caused by biofilms growing within proppant packing used in hydraulic fracturing (2, pp. 862–869). Proceedings—SPE International Symposium on Formation Damage Control, Lafayette, LA.
- Brackbill, J. U., Kothe, D. B., & Zemach, C. (1992). A continuum method for modeling surface tension. *Journal of Computational Physics*, 100(2), 335–354. [https://doi.org/10.1016/0021-9991\(92\)90240-Y](https://doi.org/10.1016/0021-9991(92)90240-Y)
- Breugem, W. P., & Boersma, B. J. (2005). Direct numerical simulations of turbulent flow over a permeable wall using a direct and a continuum approach. *Physics of Fluids*, 17(2), 1–15. <https://doi.org/10.1063/1.1835771>

- Brinkman, H. (1947). A calculation of the viscous force exerted by a flowing fluid on a dense swarm of particles. *Flow, Turbulence and Combustion*, 1(1). <https://doi.org/10.1007/bf02120313>
- Brooks, R., & Corey, A. (1964). *Hydraulic properties of porous media* (Hydrology Papers 3, p. 37). Fort Collins, CO: Colorado State University.
- Burrus, J., Kuhfuss, A., Doligez, B., & Ungerer, P. (1991). Are numerical models useful in reconstructing the migration of hydrocarbons? A discussion based on the Northern Viking Graben. *Geological Society Special Publication*, 59(1), 89–109. <https://doi.org/10.1144/GSL.SP.1991.059.01.06>
- Buscarnera, G., & Einav, I. (2012). The yielding of brittle unsaturated granular soils. *Geotechnique*, 62(2), 147–160. <https://doi.org/10.1680/geot.10.P.118>
- Carrillo, F. J., & Bourg, I. C. (2019). A Darcy-Brinkman-Biot Approach to modeling the hydrology and mechanics of porous media containing macropores and deformable microporous regions. *Water Resources Research*, 55(10), 8096–8121. <https://doi.org/10.1029/2019WR024712>
- Carrillo, F. J., & Bourg, I. C. (2020). *hybridBiotInterFoam*. <https://doi.org/10.5281/ZENODO.4013969>. Retrieved from <https://zenodo.org/record/4013969>
- Carrillo, F. J., Bourg, I. C., & Soulaine, C. (2020). Multiphase flow modelling in multiscale porous media: An open-sourced micro-continuum approach. *Journal of Computational Physics*, X, 100073. <https://doi.org/10.1016/j.jcpx.2020.100073>
- Colombo, M., & Fairweather, M. (2015). Multiphase turbulence in bubbly flows: RANS simulations. *International Journal of Multiphase Flow*, 77, 222–243. <https://doi.org/10.1016/j.ijmultiphaseflow.2015.09.003>
- Cunningham, A. B., Sharp, R. R., Hiebert, R., & James, G. (2003). Subsurface biofilm barriers for the containment and remediation of contaminated groundwater. *Bioremediation Journal*, 7(3–4), 151–164. <https://doi.org/10.1080/713607982>
- Di Donato, G., Huang, W., & Blunt, M. (2003). Streamline-based dual porosity simulation of fractured reservoirs (129, pp. 121–131). Proceedings—SPE Annual Technical Conference and Exhibition, Denver, CO. <https://doi.org/10.2523/84036-ms>
- Ehrhardt, M. (2010). An introduction to fluid-porous interface coupling. *Progress in Computational Physics*, 2, 3–12. <https://doi.org/10.2174/978160805254711202010003>
- Ferer, M., Ji, C., Bromhal, G. S., Cook, J., Ahmadi, G., & Smith, D. H. (2004). Crossover from capillary fingering to viscous fingering for immiscible unstable flow: Experiment and modeling. *Physical Review E*, 70(1), 7. <https://doi.org/10.1103/PhysRevE.70.016303>
- Ferrari, A., Jimenez-Martinez, J., Le Borgne, T., Méheust, Y., & Lunati, I. (2015). Challenges in modeling unstable two-phase flow experiments in porous micromodels. *Water Resources Research*, 51(3), 1381–1400. <https://doi.org/10.1002/2014WR016384>
- Fetzer, T., Smits, K. M., & Helmig, R. (2016). Effect of turbulence and roughness on coupled porous-medium/free-flow exchange processes. *Transport in Porous Media*, 114(2), 395–424. <https://doi.org/10.1007/s11242-016-0654-6>
- Guo, B., Ma, L., & Tchelepi, H. A. (2018). Image-based micro-continuum model for gas flow in organic-rich shale rock. *Advances in Water Resources*, 122, 70–84. <https://doi.org/10.1016/j.advwatres.2018.10.004>
- Hahn, S., Je, J., & Choi, H. (2002). Direct numerical simulation of turbulent channel flow with permeable walls. *Journal of Fluid Mechanics*, 450(1), 259–285. <https://doi.org/10.1017/s0022112001006437>
- Hassan, W. A., & Jiang, X. (2012). Upscaling and its application in numerical simulation of long-term CO₂ storage. *Greenhouse Gases: Science and Technology*, 2(6), 408–418. <https://doi.org/10.1002/ghg.1306>
- Hirt, C. W., & Nichols, B. D. (1981). Volume of Fluid (VOF) method for the dynamics of free boundaries. *Journal of Computational Physics*, 39, 201–225.
- Horgue, P., Prat, M., & Quintard, M. (2014). A penalization technique applied to the “Volume-Of-Fluid” method: Wettability condition on immersed boundaries. *Computers & Fluids*, 100, 255–266. <https://doi.org/10.1016/j.compfluid.2014.05.027>
- Howes, F. A., & Whitaker, S. (1985). The spatial averaging theorem revisited. *Chemical Engineering Science*, 40(8), 1387–1392. [https://doi.org/10.1016/0009-2509\(85\)80078-6](https://doi.org/10.1016/0009-2509(85)80078-6)
- Huang, H., Zhang, F., Callahan, P., & Ayoub, J. (2012a). Fluid injection experiments in 2D porous media. *SPE Journal*, 17, 903–911. <https://doi.org/10.2118/140502-PA>
- Huang, H., Zhang, F., Callahan, P., & Ayoub, J. (2012b). Granular fingering in fluid injection into dense granular media in a Hele-Shaw cell. *Physical Review Letters*, 108(25), 258001. <https://doi.org/10.1103/PhysRevLett.108.258001>
- Issa, R. I. (1986). Solution of the implicitly discretised fluid flow equations by operator-splitting. *Journal of Computational Physics*, 62(1), 40–65. [https://doi.org/10.1016/0021-9991\(86\)90099-9](https://doi.org/10.1016/0021-9991(86)90099-9)
- Jasak, H. (1996). *Error analysis and estimation for the finite volume method with applications to fluid flows* (Doctoral dissertation). London, UK: University of London. Retrieved from <https://spiral.imperial.ac.uk/handle/10044/1/8335>
- Jasak, H., & Weller, H. G. (2000). Application of the finite volume method and unstructured meshes to linear elasticity. *International Journal for Numerical Methods in Engineering*, 48(2), 267–287. [https://doi.org/10.1002/\(SICI\)1097-0207\(20000520\)48:2<267::AID-NME884>3.0.CO;2-Q](https://doi.org/10.1002/(SICI)1097-0207(20000520)48:2<267::AID-NME884>3.0.CO;2-Q)
- Jha, B., & Juanes, R. (2014). Coupled multiphase flow and poromechanics: A computational model of pore pressure effects on fault slip and earthquake triggering. *Water Resources Research*, 50(5), 3776–3808. <https://doi.org/10.1002/2013WR015175>
- Kang, D. H., Yang, E., & Yun, T. S. (2019). Stokes-Brinkman flow simulation based on 3-D μ -CT images of porous rock using grayscale pore voxel permeability. *Water Resources Research*, 55(5), 4448–4464. <https://doi.org/10.1029/2018WR024179>
- Kapellos, G. E., Alexiou, T. S., & Payatakes, A. C. (2007). Hierarchical simulator of biofilm growth and dynamics in granular porous materials. *Advances in Water Resources*, 30(6–7), 1648–1667. <https://doi.org/10.1016/j.advwatres.2006.05.030>
- Khadra, K., Angot, P., Parneix, S., & Caltagirone, J.-P. (2000). Fictitious domain approach for numerical modelling of Navier-Stokes equations. *International Journal for Numerical Methods in Fluids*, 34(8), 651–684. [https://doi.org/10.1002/1097-0363\(20001230\)34:8<651::AID-FLD613.0.CO;2-D](https://doi.org/10.1002/1097-0363(20001230)34:8<651::AID-FLD613.0.CO;2-D)
- Kim, J., Tchelepi, H. A., & Juanes, R. (2013). Rigorous coupling of geomechanics and multiphase flow with strong capillarity. *SPE Journal*, 18(6), 1123–1139. <https://doi.org/10.2118/141268-PA>
- Krafczyk, M., Kucher, K., Wang, Y., & Geier, M. (2015). DNS/LES Studies of Turbulent Flows Based on the Cumulant Lattice Boltzmann Approach. In W. Nagel, D. Kröner, & M. Resch (Eds.), *High Performance Computing in Science and Engineering '14*. Cham: Springer. https://doi.org/10.1007/978-3-319-10810-0_34
- Lacis, U., Zampogna, G. A., & Bagheri, S. (2017). A computational continuum model of poroelastic beds. *Proceedings of the Royal Society A: Mathematical, Physical & Engineering Sciences*, 473(2199), 20160932. <https://doi.org/10.1098/rspa.2016.0932>
- Lenormand, R., Touboul, E., & Zarcone, C. (1988). Numerical models and experiments on immiscible displacements in porous media. *Journal of Fluid Mechanics*, 189, 165–187. <https://doi.org/10.1017/S0022112088000953>
- Lenormand, R., & Zarcone, C. (1989). Capillary fingering: Percolation and fractal dimension. *Transport in Porous Media*, 4(6), 599–612. <https://doi.org/10.1007/BF00223630>

- Lo, W. C., Sposito, G., & Majer, E. (2002). Immiscible two-phase fluid flows in deformable porous media. *Advances in Water Resources*, 25(8–12), 1105–1117. [https://doi.org/10.1016/S0309-1708\(02\)00050-7](https://doi.org/10.1016/S0309-1708(02)00050-7)
- Lo, W.-C., Sposito, G., & Majer, E. (2005). Wave propagation through elastic porous media containing two immiscible fluids. *Water Resources Research*, 41(2). <https://doi.org/10.1029/2004WR003162>
- MacMinn, C. W., Dufresne, E. R., & Wetlaufer, J. S. (2016). Large Deformations of a soft porous material. *Physical Review Applied*, 5(4), 044020. <https://doi.org/10.1103/PhysRevApplied.5.044020>
- Márquez, S., & Fich, D. (2013). *An extended mixture model for the simultaneous treatment of short and long scale interfaces* (Unpublished doctoral dissertation): Universidad Nacional del Litoral.
- Mathias, S. A., Greenwell, H. C., Withers, C., Erdogan, A. R., McElwaine, J. N., & MacMinn, C. (2017). Analytical solution for clay plug swelling experiments. *Applied Clay Science*, 149, 75–78. <https://doi.org/10.1016/j.clay.2017.07.021>
- Mathieu, L., van Wyk de Vries, B., Holohan, E. P., & Troll, V. R. (2008). Dykes, cups, saucers and sills: Analogue experiments on magma intrusion into brittle rocks. *Earth and Planetary Science Letters*, 271(1–4), 1–13. <https://doi.org/10.1016/j.epsl.2008.02.020>
- Mehmani, Y., & Tchelepi, H. A. (2019). Multiscale formulation of two-phase flow at the pore scale. *Journal of Computational Physics*, 389, 164–188. <https://doi.org/10.1016/j.jcp.2019.03.035>
- Meng, Y., Primkulov, B. K., Yang, Z., Kwok, C. Y., & Juanes, R. (2020). Jamming transition and emergence of fracturing in wet granular media. *Physical Review Research*, 2(2). 022012. <https://doi.org/10.1103/physrevresearch.2.022012>
- Morris, J. P., Hao, Y., Foxall, W., & McNab, W. (2011). A study of injection-induced mechanical deformation at the In Salah CO₂ storage project. *International Journal of Greenhouse Gas Control*, 5(2), 270–280. <https://doi.org/10.1016/j.ijgac.2010.10.004>
- Morton, R. A. (2002). Factors controlling storm impacts on coastal barriers and beaches—A preliminary basis for near real-time forecasting. *Journal of Coastal Research*, 18(3), 486–501. Retrieved from <https://www.jstor.org/stable/4299096>
- Neale, G., & Nader, W. (1974). Practical significance of Brinkman's extension of Darcy's law: Coupled parallel flows within a channel and a bounding porous medium. *The Canadian Journal of Chemical Engineering*, 52(4), 475–478. <https://doi.org/10.1002/cjce.5450520407>
- Oldecop, L. A., & Alonso, E. E. (2003). Suction effects on rockfill compressibility. *Geotechnique*, 53(2), 289–292. <https://doi.org/10.1680/geot.2003.53.2.289>
- Papanastasiou, P. (2000). Hydraulic fracture closure in a pressure-sensitive elastoplastic medium. *International Journal of Fracture*, 103(2), 149–161. <https://doi.org/10.1023/A:1007634723191>
- Patankar, S. V. (1980). *Numerical heat transfer and fluid flow*, Boca Raton: CRC Press. <https://doi.org/10.13182/nse81-a20112>. Retrieved from <https://www.taylorfrancis.com/books/9781482234213>
- Qin, Z., Esmaeilzadeh, S., Riaz, A., & Tchelepi, H. A. (2020). Two-phase multiscale numerical framework for modeling thin films on curved solid surfaces in porous media. *Journal of Computational Physics*, 413, 109464. <https://doi.org/10.1016/j.jcp.2020.109464>
- Quemada, D. (1977). Rheology of concentrated disperse systems and minimum energy dissipation principle—I. Viscosity-concentration relationship. *Rheologica Acta*, 16(1), 82–94. <https://doi.org/10.1007/BF01516932>
- Räss, L., Simon, N. S., & Podlachikov, Y. Y. (2018). Spontaneous formation of fluid escape pipes from subsurface reservoirs. *Scientific Reports*, 8(1), 1–11. <https://doi.org/10.1038/s41598-018-29485-5>
- Rudman, M. (1997). Volume-tracking methods for interfacial flow calculations. *International Journal for Numerical Methods in Fluids*, 24(7), 671–691. [https://doi.org/10.1002/\(SICI\)1097-0363\(19970415\)24:7<671::AID-FLD508>3.0.CO;2-9](https://doi.org/10.1002/(SICI)1097-0363(19970415)24:7<671::AID-FLD508>3.0.CO;2-9)
- Rutqvist, J. (2012). The geomechanics of CO₂ storage in deep sedimentary formations. *Geotechnical & Geological Engineering*, 30(3), 525–551. <https://doi.org/10.1007/s10706-011-9491-0>
- Santillán, D., Mosquera, J. C., & Cueto-Felgueroso, L. (2017). Phase-field model for brittle fracture. Validation with experimental results and extension to dam engineering problems. *Engineering Fracture Mechanics*, 178, 109–125. <https://doi.org/10.1016/j.engfracmech.2017.04.020>
- Shapiro, S. A., & Dinske, C. (2009). Fluid-induced seismicity: Pressure diffusion and hydraulic fracturing. *Geophysical Prospecting*, 57(2), 301–310. <https://doi.org/10.1111/j.1365-2478.2008.00770.x>
- Shih, A. T., & Megaridis, C. M. (1996). Thermocapillary flow effects on convective droplet evaporation. *International Journal of Heat and Mass Transfer*, 39(2), 247–257. [https://doi.org/10.1016/0017-9310\(95\)00137-X](https://doi.org/10.1016/0017-9310(95)00137-X)
- Siddique, J., Ahmed, A., Aziz, A., & Khalique, C. (2017). A review of mixture theory for deformable porous media and applications. *Applied Sciences*, 7(9), 917. <https://doi.org/10.3390/app7090917>. Retrieved from <http://www.mdpi.com/2076-3417/7/9/917>
- Singh, K. (2019). How hydraulic properties of organic matter control effective liquid permeability of mudrocks. *Transport in Porous Media*, 129(3), 761–777. <https://doi.org/10.1007/s11242-019-01305-y>
- Soulaine, C., Creux, P., & Tchelepi, H. A. (2019). Micro-continuum framework for pore-scale multiphase fluid transport in shale formations. *Transport in Porous Media*, 127(1), 85–112. <https://doi.org/10.1007/s11242-018-1181-4>
- Soulaine, C., Gjetvaj, F., Garing, C., Roman, S., Russian, A., Gouze, P., & Tchelepi, H. A. (2016). The impact of sub-resolution porosity of X-ray microtomography images on the permeability. *Transport in Porous Media*, 113(1), 227–243. <https://doi.org/10.1007/s11242-016-0690-2>
- Soulaine, C., & Quintard, M. (2014). On the use of a Darcy-Forchheimer like model for a macro-scale description of turbulence in porous media and its application to structured packings. *International Journal of Heat and Mass Transfer*, 74, 88–100. <https://doi.org/10.1016/j.ijheatmasstransfer.2014.02.069>
- Soulaine, C., Roman, S., Kovsek, A., & Tchelepi, H. A. (2017). Mineral dissolution and wormholing from a pore-scale perspective. *Journal of Fluid Mechanics*, 827, 457–483. <https://doi.org/10.1017/jfm.2017.499>
- Spearman, J. (2017). An examination of the rheology of flocculated clay suspensions. *Ocean Dynamics*, 67(3–4), 485–497. <https://doi.org/10.1007/s10236-017-1041-8>
- Tentner, A., Lo, S., Sławski, A., Loilev, A., Melnikov, V., Samigulin, M., et al. (2008). *Computational fluid dynamics modeling of two-phase flow topologies in a boiling water reactor fuel assembly* (3, pp. 430–440). International Conference on Nuclear Engineering, Proceedings, ICONE, American Society of Mechanical Engineers Digital Collection. <https://doi.org/10.1115/ICONE16-48442>
- Terzaghi, K. (1943). *Theoretical soil mechanics*. Hoboken, NJ: John Wiley & Sons, Inc. <https://doi.org/10.1002/9780470172766>
- Terzaghi, K., Peck, R. B., & Mesri, G. (1996). *Soil mechanics in engineering practice*, Hoboken, NJ: John Wiley & Sons, Inc.
- Towner, G. D. (1987). The mechanics of cracking of drying clay. *Journal of Agricultural Engineering Research*, 36(2), 115–124. [https://doi.org/10.1016/0021-8634\(87\)90118-1](https://doi.org/10.1016/0021-8634(87)90118-1)
- van Dam, D. B., Papanastasiou, P., & de Pater, C. J. (2002). Impact of rock plasticity on hydraulic fracture propagation and closure. *SPE Production and Facilities*, 17(3), 149–159. <https://doi.org/10.2118/78812-PA>
- van Genuchten, M. T. (1980). A Closed-form equation for predicting the hydraulic conductivity of unsaturated soils. *Soil Science Society of America Journal*, 44(5), 892–898. <https://doi.org/10.2136/sssaj1980.03615995004400050002x>

- Verruijt, A. (2013). *Theory and problems of poroelasticity*. Delft, The Netherlands: Delft University of Technology.
- Von Mises, R. (1913). Mechanics of solid bodies in the plastically-deformable state. *Mathematisch-Physikalischen Klasse*, 4, 1–10.
- Wan, R., Khosrovani, S., & Pourgha, M. (2014). Micromechanical analysis of force transport in wet granular soils. *Vadose Zone Journal*, 13(5). vjz2013.06.0113. <https://doi.org/10.2136/vzj2013.06.0113>
- Weishaupt, K., Joekar-Niasar, V., & Helmig, R. (2019). An efficient coupling of free flow and porous media flow using the pore-network modeling approach. *Journal of Computational Physics: X*, 1, 100011. <https://doi.org/10.1016/j.jcpx.2019.100011>
- Whitaker, S. (1986). Flow in porous media I: A theoretical derivation of Darcy's law. *Transport in Porous Media*, 1(1), 3–25. <https://doi.org/10.1007/BF01036523>
- Whitaker, S. (1999). The method of volume averaging (1). Dordrecht, The Netherlands: Springer. <https://doi.org/10.1007/978-94-017-3389-2>
- Whitaker, S. (2013). Volume averaging of transport equations. *Fluid Transport in Porous Media*, 53(9), 1689–1699. Retrieved from https://www.researchgate.net/publication/253952986_Volume_Averaging_of_Transport_Equations
- Zampogna, G. A., Lácis, U., Bagheri, S., & Bottaro, A. (2019). Modeling waves in fluids flowing over and through poroelastic media. *International Journal of Multiphase Flow*, 110, 148–164. <https://doi.org/10.1016/j.ijmultiphaseflow.2018.09.006>